State-resolved Photodissociation and Radiative Association Data for the Molecular Hydrogen Ion

Mark C. Zammit[1], Jeremy S. Savage[2], James Colgan[1] , Dmitry V. Fursa[2], David P. Kilcrease[1] , Igor Bray[2] ,
Christopher J. Fontes[1] , Peter Hakel[1] , and Eddy Timmermans[1]
[1] Los Alamos National Laboratory, Los Alamos, NM 87545, USA; mzammit@lanl.gov
[2] Curtin Institute for Computation and Department of Physics, Astronomy and Medical Radiation Sciences, Curtin University,
Perth, Western Australia 6102, Australia

Abstract

We present state-resolved (electronic, vibrational, and rotational) cross sections and rate coefficients for the photodissociation (PD) of H_2^+ and radiative association (RA) of H–H^+. We developed a fully quantum mechanical approach within the nonrelativistic Born–Oppenheimer approximation to describe H_2^+ and calculate the data for transitions between the ground electronic state $1s\sigma_g$ and the $2p\sigma_u$, $2p\pi_u$, $3p\sigma_u$, $3p\pi_u$, $4p\sigma_u$, $4f\sigma_u$, $4f\pi_u$, and $4p\pi_u$ electronic states (i.e., up to H_2^+ $n = 4$). Tables of the dipole-matrix elements and energies needed to calculate state-resolved cross sections and rate coefficients will be made publicly available. These data could be important in astrophysical models when dealing with photon wavelengths (or radiation temperature distributions that are weighted toward such wavelengths) around 100 nm. For example, at these wavelengths and a material temperature of 8400 K, the LTE-averaged PD cross section via the (second electronically excited) $2p\pi_u$ state is over three times larger than the PD cross section via the (first electronically excited) $2p\sigma_u$ state.

Key words: early universe – galaxies: star formation – molecular data – molecular processes

1. Introduction

The molecular hydrogen ion H_2^+ and its isotopologues (D_2^+, T_2^+, HD^+, HT^+, and DT^+) are among the most abundant molecular ions in the universe (Lepp et al. 2002) and play important roles in determining the dynamics of astrophysical and laboratory-produced low-temperature hydrogen plasmas (Janev et al. 2003), where, for example, molecules are abundant on the edge of magnetically confined plasmas and in the divertor region. Studies of these plasmas in both local thermodynamic equilibrium (LTE) and non-LTE require state-resolved (electronic, vibrational, and rotationally resolved) transition cross sections or rate coefficients to calculate populations (for non-LTE plasmas), opacities, and emissivities. Recent studies of the H_2 chemistry in the early universe suggest that LTE conditions may not apply for H_2^+ at low temperatures (Hirata & Padmanabhan 2006; Longo et al. 2011; Sugimura et al. 2016), further indicating the need for state-resolved H_2^+ data. State-resolved and summed photon–H_2^+ data have been utilized in a range of models of the early universe's chemistry (Galli & Palla 1998; Stancil et al. 1998; Lepp et al. 2002; Hirata & Padmanabhan 2006; Coppola et al. 2011), gas clouds chemistry (Ferland et al. 2013; Lykins et al. 2015; Coppola et al. 2016; Sugimura et al. 2016), solar atmospheres (Stancil 1994b; Mihajlov et al. 2007), and the opacity of primordial matter (Mayer & Duschl 2005). In addition, H–H^+ collision-induced absorption effects (or quasi-molecular transitions) have been investigated to model Lyman satellites in the context of DA white dwarf atmospheres, old horizontal-branch stars of spectral type A, and λ Bootis stars (Allard et al. 1998, 2000, 2009; Santos & Kepler 2012; Pelisoli et al. 2015).

The absence of state-resolved data for H_2^+ was noted recently in the literature by Coppola et al. (2011), Glover et al. (2014), and Babb (2015). Babb (2015) addressed this lack of data for the low-lying states and presented state-resolved dipole-matrix

elements for the radiative association (RA) process,

$$H(nl) + H^+ \rightarrow H_2^+(1s\sigma_g, v, N) + \gamma(\lambda_\gamma), \quad (1)$$
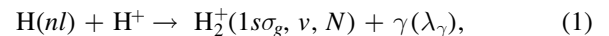
via the $H(1s)$ state and the inverse process, photodissociation (PD),

$$\gamma(\lambda_\gamma) + H_2^+(1s\sigma_g, v, N) \rightarrow H_2^{+*}$$
$$\rightarrow H^+ + H(nl), \quad (2)$$
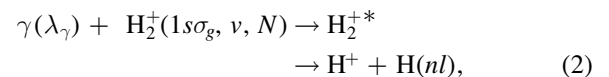
via the first electronically excited state $H_2^+(2p\sigma_u)$, producing $H(1s)$. Babb (2015) calculated these dipole-matrix elements for each vibrational quantum number v and angular momentum N as a function of the photon γ wavelength λ_γ.

In principle, however, reaction (1) can occur via all excited states of H, and reaction (2) can occur via (almost) all electronically excited states of H_2^+ (Dance et al. 1967; Dunn & Van Zyl 1967; Peek 1974) and the vibrational continuum of the electronic ground state, which are represented collectively as H_2^{+*} in Equation (2). In Figure 1, we present the low-lying potential energy curves of H_2^+ computed by methods described in Section 2.1. Here we take the H_2^+ state labels from the respective united atom limit (He^+) states. By analyzing the individual transition contributions to the static dipole polarizability of the H_2^+ ground state, one finds that the $2p\sigma_u$ and $2p\pi_u$ states dominate the static dipole polarizability, contributing approximately 61% and 34% of the total polarizability, respectively. As pointed out by Saha et al. (1980), the PD cross section of the $2p\pi_u$ state at 100 nm is approximately 1.7 times larger than that for the $2p\sigma_u$ state when assuming a (near) Franck–Condon (FC) distribution of H_2^+ (produced from ionization of the H_2 ground state; von Busch & Dunn 1972). Hence, considering PD beyond the "two-level" approximation for H_2^+ is likely to be important for photon wavelengths (or radiation temperature distributions that are weighted toward wavelengths) around 100 nm. As is the case for H_2 (Latter &
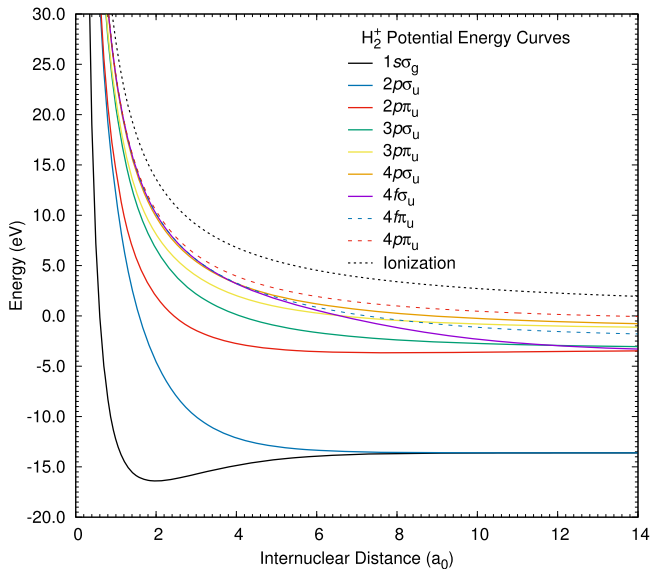
Figure 1. Potential energy curves of H_2^+ for the ground electronic state $1s\sigma_g$ up to the $n = 4$ H_2^+ dipole-allowed transition states, i.e., $2p\sigma_u$, $2p\pi_u$, $3p\sigma_u$, $3p\pi_u$, $4p\sigma_u$, $4f\sigma_u$, $4f\pi_u$, and $4p\pi_u$, where the labels are taken from the respective united atom limit states (He^+).

Black 1991), HeLi$^+$ (Zámečníková et al. 2017), and He_2^+ (Augustovičová et al. 2013a, 2013b), it may also be important to consider RA (1) via the excited states of atomic H, as the RA cross section is proportional to the released photon energy cubed, i.e., $\sigma^{RA} \propto E_\gamma^3$. For example, RA via the [H(2p)+H$^+$]($2p\pi_u$) channel releases a higher-energy photon compared to RA via the [H(1s)+H$^+$]($2p\sigma_u$) channel.

As far as we are aware, astrophysical plasma models that include H_2^+ molecules only consider PD processes in the "two-level" approximation (via the $2p\sigma_u$ state), even at wavelengths around 100 nm (Stancil et al. 1993; Stancil 1994b; Mihajlov et al. 2007; Sugimura et al. 2016). It is also important to note that in reaction (2), the final state of the dissociating H atom is dependent on the dissociating pathway of H_2^{+*}. For example, PD of H_2^+ via the $2p\sigma_u$ state leaves the dissociating H atom in the 1s state, and PD via the $2p\pi_u$ state leaves the dissociating H atom in the 2p state. This distinction of the asymptotic final states of atomic H could be important in non-LTE plasma models and collisional-radiative models, where the excited H atom could emit a photon or undergo a collision (particularly when atomic H is formed in its metastable 2s state). Refer to Table 2 for the H_2^+ states that lead to the separated atomic states.

The fundamental γ–H_2^+ system has been studied extensively. Classic works on the H_2^+ structure were conducted by Bates et al. (1953b), who solved the electronic structure problem of H_2^+ utilizing prolate-spheroidal coordinates, and Madsen & Peek (1971), who presented the potential energy curves of 20 electronic states of H_2^+ (or up to atomic [H($n \leqslant 3$)+H$^+$] in the separated atom limit). Similarly, these authors presented oscillator strengths as a function of the internuclear distance R for various transitions (Bates 1951a; Bates et al. 1953a, 1954), with the most comprehensive set presented by Ramaker & Peek (1973) for transitions between states in the [H($n \leqslant 3$) + H$^+$] system. More recently, oscillator strengths have been presented as a function of R by Babb (1994) and Tsogbayar & Banzragch (2010) for low-lying transitions, while comprehensive calculations have been performed by Allard

et al. (2009) for $n = 1, 2 \rightarrow 5, 6, 7, 8$ transitions of H_2^+ and Santos & Kepler (2012) for transitions up to the $n \leqslant 10$ states of H_2^+. Vibrationally weighted PD cross sections of H_2^+ via the $2p\sigma_u$ and $2p\pi_u$ states were presented by Saha et al. (1980) and compared well with the experiment of von Busch & Dunn (1972). Igarashi (2014) presented the H_2^+ ground-state PD cross section for the final dissociative [H($n \leqslant 4$)+H$^+$] states. Perhaps the most complete quantum mechanical study was performed by Haxton (2013), who investigated the difference between utilizing the Born–Oppenheimer approximation and the exact nonadiabatic method in the calculation of the H_2^+ ground-state PD and photoionization cross sections. Haxton (2013) confirmed the accuracy of utilizing the Born–Oppenheimer approximation in calculating PD and photoionization cross sections differential in energy. The RA via [H(1s)+H$^+$] has been presented for the total cross section by Stancil et al. (1993) and the rate coefficient by Ramaker & Peek (1976) and Stancil et al. (1993). The LTE-weighted PD cross sections via the $2p\sigma_u$ state have been presented by Argyros (1974), Stancil (1994b), Lebedev & Presnyakov (2002), and Lebedev et al. (2003). State-resolved data of the γ–H_2^+ system have only been presented for the PD and RA processes via the $2p\sigma_u$ state by Dunn (1968) and Babb (2015) and in the database MOL-D (Vujčić et al. 2015). As far as we are aware, state-resolved γ–H_2^+ data have not been presented for electronic states higher than the $2p\sigma_u$ state.

In this paper, we first present the state-resolved static dipole polarizability of H_2^+ and quantitatively determine the major electronic transition contributions. We then formulate and present state-resolved PD and RA cross sections for H_2^+ via the first eight dipole-allowed electronic states (i.e., up to H_2^+ $n = 4$): $2p\sigma_u$, $2p\pi_u$, $3p\sigma_u$, $3p\pi_u$, $4p\sigma_u$, $4f\sigma_u$, $4f\pi_u$, and $4p\pi_u$. Comprehensive state-resolved dipole-matrix element tables will be made publicly available. With these tables, cross sections can be assembled and summed or averaged as required for applications in calculating rate coefficients for LTE or non-LTE plasma models. We make various comparisons with previous theoretical works and measurements of the PD and RA cross sections. We also present selected partition functions and energy levels of H_2^+.

2. Method

We utilize the notation variables X and Y to indicate the different nuclei within the molecule. Molecular state labels correspond to the respective united atom state labels. Here [H(nl)+H$^+$]($n'l'm_\pi$) refers to H in the asymptotic electronic state nl, which goes along the H_2^+ potential energy curve $n'l'm_\pi$. All equations are formulated in atomic units unless explicitly stated.

2.1. Molecular States

Here we give a brief overview of the formulation of the molecular states and calculation of the dipole-matrix elements; a detailed discussion is given in the Appendix. The molecular states $\bar{\Phi}_{nvNm_N}(\boldsymbol{x}, \boldsymbol{R})$ are formulated within the nonrelativistic Born–Oppenheimer approximation

$$\bar{\Phi}_{nvNm_N}(\boldsymbol{x}, \boldsymbol{R}) \approx \Phi_n(\boldsymbol{x}; \boldsymbol{R})\nu_{nvN}(R)R_{nNm_N}(\hat{\boldsymbol{R}}), \qquad (3)$$

where $\boldsymbol{x}$ represents the spatial and spin coordinates of the electron and $\boldsymbol{R}$ represents the spatial coordinates of the nuclei. The H_2^+ electronic states $\Phi_n(\boldsymbol{x}; \boldsymbol{R})$ are characterized by the electronic orbital angular momentum projection m_n, parity π_n,

and spin s_n (with $s_n = 1/2$). The vibrational wave functions $\nu_{nvN}(R)$ are characterized by the vibrational quantum number v and rotational quantum number N (total angular momentum excluding electron spin). The rotational wave functions $R_{nNm_N}(\hat{R})$ can be factored out of the total molecular dipole-matrix elements and reentered into the cross sections via the so-called Hönl–London factors (Whiting & Nicholls 1974; Hansson & Watson 2005; Watson 2008). Here the nuclei-spin wave functions have been factored out of the molecular states (3). They reenter the cross sections as an overlap matrix and play a role in the symmetry of the total wave function and the allowed molecular states of the homonuclear diatomic molecules (H_2^+, D_2^+, and T_2^+), which is particularly important in the calculation of the partition functions (Herzberg 1950).

A modified prolate-spheroidal coordinate system is used to formulate electronic wave functions and calculate electronic dipole-matrix elements $\mathcal{M}_{f,i}(R)$. For each internuclear separation R and combination of (m, π, s), we diagonalize the body (molecular fixed) frame electronic Hamiltonian in a set of one-electron orbitals $\{\phi_j\}$ constructed from Sturmian Hylleraas functions to obtain energies $\varepsilon(R)$ (eigenvalues) and expansion coefficients $C_j(R)$ (eigenvectors). Once these are obtained, electronic target states are constructed from the Sturmian Hylleraas functions. Because the electronic H_2^+ Schrödinger equation is separable in spheroidal coordinates for a given value of R, this procedure gives practically exact electronic wave functions for calculations that utilize a very large Hylleraas basis, which forms a (near) complete expansion. Once the electronic wave functions are obtained, electronic dipole-matrix elements are calculated for this value of R. The above procedure is repeated over a range of internuclear separations R up to a maximum internuclear separation R_{max}. Interpolating over R, the Born–Oppenheimer potential energy curves $\varepsilon_n(R)$ (as defined by Bishop & Cheung 1977 and shown in Figure 1) and electronic dipole-matrix-element surfaces $\mathcal{M}_{f,i}(R)$ are obtained.

For a diatomic molecule in an electronic state n, the nonrelativistic Born–Oppenheimer Hamiltonian for the vibrational motion is given by Beckel et al. (1973),

$$H_n^{BO}(R) = -\frac{1}{2\mu}\frac{d^2}{dR^2} + \frac{N(N+1) - m_n^2}{2\mu R^2} + V_n(R), \quad (4)$$

where μ is the reduced mass of the nuclei given in Section 2.3. To obtain the bound vibrational wave functions $\nu_{nvN}(R)$, for each electronic state n and rotational quantum number N, we diagonalize the above Hamiltonian (Equation (4)) with $V_n(R) = \varepsilon_n(R)$ in a set of nuclear orbitals constructed from (Sturmian) Laguerre basis functions (Zammit et al. 2013, 2014, 2017a). This basis is taken to convergence, and only the bound vibrational wave functions are retained.

The energy-normalized distorted continuum vibrational wave functions $\nu_{nE_kN}(R)$ are obtained by solving the vibrational Schrödinger equation for the above Hamiltonian (Equation (4)) with $V_n(R) = \varepsilon_n(R) - \mathcal{D}_n$, where $\mathcal{D}_n$ is the energy of the asymptotic electronic state n (i.e., separated atom limit). The values for $\mathcal{D}_n$ are given in Table 2. We utilize the Numerov method to obtain energy-normalized continuum wave

functions, which have the asymptotic form

$$\nu_{nE_kN}(R) \underset{R\to\infty}{\longrightarrow} \sqrt{\frac{2\mu}{k\pi}}\frac{1}{R}\sin(kR - \pi N/2 + \delta(n, N)) \quad (5)$$

and satisfy

$$\int_0^\infty R^2 \nu_{nE_kN}(R)\nu_{nE_{k'}N}(R)dR = \delta(E_k - E_{k'}), \quad (6)$$

where $k = \sqrt{2\mu E_k}$ (the momentum associated with the relative velocity of the nuclei) and $\delta(n, N)$ is a phase shift.

Finally, the (symmetric) electronic-vibrational dipole-matrix elements are calculated for bound–free and bound–bound transitions via

$$\mathcal{M}_{fE_{k_f}N_f, iv_iN_i} = \langle \nu_{fE_{k_f}N_f}|\mathcal{M}_{f,i}|\nu_{iv_iN_i}\rangle_R \text{ and} \quad (7)$$

$$\mathcal{M}_{fv_fN_f, iv_iN_i} = \langle \nu_{fv_fN_f}|\mathcal{M}_{f,i}|\nu_{iv_iN_i}\rangle_R, \quad (8)$$

respectively. For these dipole transitions, e.g., $iv_iN_i \to fE_{k_f}N_f$, we assume that the vibrational wave functions satisfy the approximate relationship

$$|n, v, N\rangle \approx |n, v, N+1\rangle \approx |n, v, N-1\rangle, \quad (9)$$

where, for a dipole transition, $N_f = N_i, N_i \pm 1$. It is important to note that for an electronic state n, molecular states only exist for $N \geqslant m_n$ (Brown & Carrington 2003). Hence, it is a good approximation to take the dipole-matrix elements as

$$\mathcal{M}_{fE_{k_f}N, iv_iN_i} \approx \begin{cases} \mathcal{M}_{fE_{k_f}(N_i+1), iv_iN_i}, & N_i < m_f \\ \mathcal{M}_{fE_{k_f}N_i, iv_iN_i}, & N_i \geqslant m_f \end{cases}. \quad (10)$$

The approximations given in Equations (9) and (10) are commonly utilized (Babb 2015) in order to produce compact data tables. In the calculation of the dipole-matrix elements, we apply the dipole selection rules ($g \leftrightarrow u$, $N_f = N_i, N_i \pm 1$, and $m_f = m_i, m_i \pm 1$).

2.2. State-resolved Static Dipole Polarizability

The total static dipole polarizability $\alpha_{iv_iN_i}$ (Mitroy et al. 2010) of a diatomic molecule in the initial electronic state i, vibrational state v_i, and rotational state N_i can be calculated from a classical approach with the parallel $\alpha_{iv_iN_i}^{\parallel}$ and perpendicular $\alpha_{iv_iN_i}^{\perp}$ components (Dalgarno & Lewis 1957; Victor & Dalgarno 1969; Bishop & Cheung 1978; Bishop 1990) such that

$$\alpha_{iv_iN_i} = \frac{1}{3}\alpha_{iv_iN_i}^{\parallel} + \frac{2}{3}\alpha_{iv_iN_i}^{\perp}. \quad (11)$$

Using the approximations in Equations (9) and (10) and assuming the molecular state energy levels satisfy the relationship

$$\varepsilon_{nvN} \approx \varepsilon_{nv(N+1)} \approx \varepsilon_{nv(N-1)}, \quad (12)$$

leading to the static dipole polarizability form given by Bishop (1990):

$$\alpha_{iv_iN_i}^{\parallel,\perp} = 2\sum_{n,v_n}\!\!\!\!\!\int g_n^{\parallel,\perp}\frac{\langle\nu_{nv_nN}|\mathcal{M}_{n,i}|\nu_{iv_iN_i}\rangle_R^2}{\varepsilon_{nv_nN} - \varepsilon_{iv_iN_i}}. \quad (13)$$

Here ν_{nvN} represents both the bound and continuum vibrational wave functions; the sum and integration are over parallel or perpendicular electronic states n only, with $g_n^{\parallel}=\delta_{m_n,0}$ and $g_n^{\perp}=\delta_{m_n,1}$, respectively. The integration is over the electronic and vibrational continuum, which is generally included via a sum over positive energy (Sturmian) pseudostates obtained from a diagonalization procedure. These positive energy pseudostates provide a discretized representation of the target continuum and form a quadrature rule. Approach (13) however, is computationally and numerically demanding, particularly for H_2^+. This is due to the large contribution from the vibrational continuum (dissociation channels) and the integration over highly oscillatory functions. In addition, the contribution from the numerous electronically excited vibrational bound states can be significant.

A commonly utilized semiclassical approximation is to calculate the fixed-nuclei static dipole polarizability and average over the initial vibrational level via (Bishop & Cheung 1979, 1980; Bishop et al. 1980; Bishop 1990)

$$\alpha_{iv_iN_i}^{\parallel,\perp} = 2\sum_n \int g_n^{\parallel,\perp} \langle \nu_{iv_iN_i}| \frac{|\mathcal{M}_{n,i}(R)|^2}{\varepsilon_n(R) - \varepsilon_i(R)}|\nu_{iv_iN_i}\rangle_R. \qquad (14)$$

However, this semiclassical approach can lead to unphysical poles when the initial electronic state potential energy curve crosses with another (dipole-allowed) electronic state potential energy curve (Bishop & Cheung 1980). This is indeed true for the H_2^+ $1s\sigma_g$ and $2p\sigma_u$ states at large internuclear separations.

Hence, to overcome the issues mentioned above, we calculate the static dipole polarizability components utilizing both approaches (13) and (14). Checking the individual-state contributions to the total static dipole polarizability via approaches (13) and (14), we found that both methods agreed to within 1% for all electronic states up to $n = 4$ of H_2^+ (not including the $2p\sigma_u$ state) for all $N_i = 0$ bound vibrational states v_i. Combining Equations (13) and (14), we calculate the total static dipole polarizability components via

$$\alpha_{iv_iN_i}^{\parallel,\perp} = 2\Bigg(\sum_{\overline{n,v_n}}^{\mathcal{N}_0} g_n^{\parallel,\perp} \frac{\langle \nu_{nv_nN}|\mathcal{M}_{n,i}|\nu_{iv_iN_i}\rangle_R^2}{\varepsilon_{nv_nN} - \varepsilon_{iv_iN_i}}$$
$$+\sum_{\overline{n}=\mathcal{N}_0+1}^{\mathcal{N}} g_n^{\parallel,\perp} \langle \nu_{iv_iN_i}| \frac{|\mathcal{M}_{n,i}(R)|^2}{\varepsilon_n(R) - \varepsilon_i(R)}|\nu_{iv_iN_i}\rangle_R \Bigg), \qquad (15)$$

where the first term sums over all $\mathcal{N}_0$ electronic states that have potential energy curves that cross with the initial electronic state (i.e., $2p\sigma_u$). The second term includes all other electronic states ($n = \mathcal{N}_0 + 1$ to $n = \mathcal{N}$), including the electronic (and the respective vibrational) continuum. Here we include the electronic continuum in the second term via the use of Sturmian pseudostates obtained from the diagonalization procedure described in Section 2.1. The integration over the vibrational continuum in the first term is performed using a Simpson's (energy grid) integration rule and energy-normalized distorted continuum vibrational wave functions.

2.3. Photodissociation and Radiative Association Cross Sections

In the dipole approximation, the PD (analogous to photoionization; Sobel'man 1972) cross section σ^{PD} is given as

$$\sigma_{fE_{k_f}N_f,iv_iN_i}^{\mathrm{PD}}(E_\gamma) = \frac{4\pi^2 E_\gamma}{3c} \frac{1}{(2N_i+1)(2s_i+1)(2-\delta_{m_i,0})}$$
$$\times \sum_{J_f,p_f,p_i} \sum_{J_i=|N_i-s_i|}^{|N_i+s_i|} |\mathcal{M}_{fE_{k_f}N_f,iv_iN_i}|^2 \mathcal{S}_{J_fN_fp_fm_fs_f,J_iN_ip_im_is_i}^{\mathrm{H\,(b)}}, \qquad (16)$$

where E_γ is the photon energy, c is the speed of light, s_i is the initial electron-state spin, and $\mathcal{M}_{fE_{k_f}N_f,iv_iN_i}$ is the dipole-matrix element given in Equation (7). The Hönl–London factors in Hund's coupling case (b) $\mathcal{S}_{J_fN_fp_fm_fs_f,J_iN_ip_im_is_i}^{\mathrm{H\,(b)}}$ are given by Hansson & Watson (2005) and Watson (2008), where J is the total angular momentum of the molecule and p is the parity of the molecular state. We note that, by definition, the Hönl–London factors analytically sum over initial and final degenerate rotational sublevels m_J, and that special care must be taken with the Hönl–London factors when calculating completely state-resolved transitions (Whiting & Nicholls 1974; Hansson & Watson 2005; Watson 2008). Utilizing the approximations summarized in Equations (9) and (10) and analytically summing over all final rotational transitions for a given initial rotational level N_i with the Hönl–London factors' property (for Hund's coupling case (b); Whiting & Nicholls 1974; Hansson & Watson 2005; Watson 2008),

$$\sum_{J_f,N_f,p_f,p_i} \sum_{J_i=|N_i-s_i|}^{|N_i+s_i|} \mathcal{S}_{J_fN_fp_fm_fs_f,J_iN_ip_im_is_i}^{\mathrm{H\,(b)}}$$
$$=(2-\delta_{0,m_f}\delta_{0,m_i})(2s_i+1)(2N_i+1), \qquad (17)$$

the final form of the cross sections is given by Babb (2015), van Dishoeck & Dalgarno (1983), and van Dishoeck (1987):

$$\sigma_{fE_{k_f},iv_iN_i}^{\mathrm{PD}}(E_\gamma) = \frac{4\pi^2 E_\gamma}{3c} \frac{(2-\delta_{0,m_f}\delta_{0,m_i})}{(2-\delta_{0,m_i})}$$
$$\times|\mathcal{M}_{fE_{k_f}N,iv_iN_i}|^2. \qquad (18)$$

As expressed in the approximation given by Equation (10), for $N_i < m_f$, we take $N = N_i + 1$, otherwise we have $N = N_i$. Similarly utilizing the approximations summarized in Equations (9) and (10), the direct RA cross section for a given rotational channel N_i (or final state N_f) is given by (Gianturco & Giorgi 1997; Babb & Kirby 1998; Babb 2015)

$$\sigma_{fv_fN_f,iE_{k_i}}^{\mathrm{RA}}(E_{k_i}) = \frac{4\pi^2 E_\gamma^3}{3c^3\mu E_{k_i}} \frac{(2-\delta_{0,m_f}\delta_{0,m_i})}{(2-\delta_{0,m_i})}$$
$$\times(2N+1)g_p \ |\mathcal{M}_{fv_fN_f,iE_{k_i}N}|^2, \qquad (19)$$

where, following Equation (10), for $N_f < m_i$, we take $N = N_f + 1$, otherwise we have $N = N_f$. Here $E_{k_i} = k_i^2/2\mu$ is the initial (relative) kinetic energy of the nuclei, and g_p is the probability of approach for the electronic states (Bates 1951b,

$$g_p(nlm_\pi) = \frac{(2s_i + 1)(2 - \delta_{0,m_i})}{\sum_n (2s_n + 1)(2 - \delta_{0,m_n})}, \quad (20)$$

where n is a sum over all the molecular electronic states that dissociate to the same separated ion–atom (or atom–atom) state. The photon energy E_γ and nuclei continuum wave function energy E_{k_f} in Equation (18) and E_{k_i} in Equation (19) are related by

$$E_\gamma = E_{k_f} + (\mathcal{D}_f - \varepsilon_{iv_iN_i}) = E_{k_i} + (\mathcal{D}_i - \varepsilon_{fv_fN_f}). \quad (21)$$

The nuclei-spin symmetry weighting has been neglected here and can be included if the cross sections are being folded into a temperature distribution (Stancil 1994b).

Following Babb (2015), cross sections can also be constructed in units of cm². For PD, we have

$$\sigma^{PD}_{fE_{k_f}, iv_iN_i}(\lambda_\gamma) = 2.689 \times 10^{-18} \left(\frac{45.563}{\lambda_\gamma} \right)$$

$$\times \frac{(2 - \delta_{0,m_f}\delta_{0,m_i})}{(2 - \delta_{0,m_i})} |\mathcal{M}_{fE_{k_f}N, iv_iN_i}|^2 \quad \text{cm}^2, \quad (22)$$

and for the RA cross section,

$$\sigma^{RA}_{fv_fN_f, iE_{k_i}}(E_{k_i}) = 1.432 \times 10^{-22} \left(\frac{45.563}{\lambda_\gamma} \right)^3$$

$$\times \frac{(2 - \delta_{0,m_f}\delta_{0,m_i})}{(2 - \delta_{0,m_i})} \frac{(2N + 1)}{\mu E_{k_i}} g_p |\mathcal{M}_{fv_fN_f, iE_{k_i}N}|^2 \quad \text{cm}^2, \quad (23)$$

where the photon wavelength λ_γ is in nm and μ, E_{k_i}, and $\mathcal{M}_{fE_{k_f}N, iv_iN_i}$ (Equation (10)) are in atomic units. The reduced mass of the nuclei $\mu = M_1 M_2 / (M_1 + M_2)$, where M_i is the mass of the individual nuclei; $M_i = 1836.152$ for a proton. For the present states considered, the probability of approach g_p is given in Table 2. We note that the RA cross section prefactor constant given in Equation (9) of Babb (2015) was recently corrected (J. Babb 2017, private communication).

2.4. LTE Populations, Partition Function, and Total LTE Cross Sections

The total LTE PD cross section as a function of material temperature T_{mat} and photon wavelength for an XY^+ molecular gas is given by

$$\sigma^{PD}_{fE_{k_f}}(\lambda_\gamma, T_{mat}; XY^+)$$

$$= \sum_{iv_iN_i} p_{n_iv_iN_i}(T_{mat}; XY^+) \sigma^{PD}_{fE_{k_f}, iv_iN_i}(\lambda_\gamma; XY^+). \quad (24)$$

For plasmas in LTE, molecular states have a population probability

$$p_{nvN}(T_{mat}; XY^+) = \frac{g_{nvN}(XY^+) \exp\left(-\frac{\varepsilon_{n_0v_0N_0} - \varepsilon_{nvN}}{k_B T_{mat}}\right)}{\mathcal{Q}_{XY^+}(T_{mat})}, \quad (25)$$

where $\mathcal{Q}_{XY^+}(T_{mat})$ is the partition function

$$\mathcal{Q}_{XY^+}(T_{mat}) = \sum_{nvN} g_{nvN}(XY^+) \exp\left(-\frac{\varepsilon_{n_0v_0N_0} - \varepsilon_{nvN}}{k_B T_{mat}}\right), \quad (26)$$

Table 1
The Nuclei-spin Statistical Weights $\tilde{g}_{nvN}(H_2^+)$ of H_2^+

	N	$\tilde{g}_{nvN}(H_2^+)$
σ_g	even	$(2S_X + 1)S_X$
σ_g	odd	$(2S_X + 1)(S_X + 1)$
σ_u	even	$(2S_X + 1)(S_X + 1)$
σ_u	odd	$(2S_X + 1)S_X$

$g_{nvN}(XY^+)$ are the statistical weights (Herzberg 1950; Stancil 1994a)

$$g_{nvN}(XY^+) = \frac{(2N + 1)(2s + 1)(2 - \delta_{m_n,0})\tilde{g}_{nvN}(XY^+)}{(2S_X + 1)(2S_Y + 1)}, \quad (27)$$

$\varepsilon_{n_0v_0N_0}$ is the ground-state energy, S_X and S_Y are the nuclei spin, and $\tilde{g}_{nvN}(H_2^+)$ is the nuclei-spin statistical weight given in Table 1. It is important to note the symmetry requirements of the molecular system and its effect on the statistical weights. Here H^+ is a fermion (with spin $S_X = 1/2$); hence, the total molecular wave function of the diatomic molecule needs to be antisymmetric (Herzberg 1950). Note that it is convention to divide the statistical weight (partition function) by the total nuclei-spin statistical weight $(2S_X + 1)(2S_Y + 1)$ (Stancil et al. 1993; Stancil 1994a). Generally, only the ground electronic state is included in the molecular partition function (Equation (26); Stancil 1994a, 1994b), and we follow the same convention. We will investigate the effect of including the electronically excited bound states elsewhere.

In experiments, a beam of H_2^+ is generally produced by electron-impact ionization of the H_2 ground state, which forms H_2^+ in a range of rovibrationally excited states. Because H_2^+ is a homonuclear diatomic molecule, rovibrational dipole transitions within the ground electronic state are forbidden; hence, these rovibrationally excited states have long lifetimes. The H_2^+ beam population distribution can therefore be assumed to be in the appropriate FC distribution (Zammit et al. 2014) or can be explicitly measured (Ghazaly et al. 2004) or inferred from experiments (von Busch & Dunn 1972). In the H_2^+ PD measurements of von Busch & Dunn (1972), they inferred the vibrational population of their beam, which we hereafter refer to as BD weights. To compare PD cross sections with experiments, the appropriate FC factors or BD weights can be substituted into p_{nvN} in Equation (24).

2.5. Rate Coefficients

The total RA cross section is given by

$$\sigma^{RA}_{f, iE_{k_i}}(E_{k_i}; XY^+) = \sum_{N_f, v_f} \sigma^{RA}_{fv_fN_f, iE_{k_i}}(E_{k_i}; XY^+). \quad (28)$$

Assuming a Maxwellian distribution of the ion velocity and atom velocity described by the effective temperature T, the rate

Table 2
The Probability of Approach g_p (Equation (20)) and the Asymptotic Electronic Energy of the [H(nl)+H$^+$]($n'l'm_\pi$) System $\mathcal{D}_n$ (in units of eV) for the $1s\sigma_g$, $2p\sigma_u$, $2p\pi_u$, $3p\sigma_u$, $3p\pi_u$, $4p\sigma_u$, $4f\sigma_u$, $4f\pi_u$, and $4p\pi_u$ Potential Energy Curves

United Atom Label	Separated Atom Label	Present $\mathcal{D}_n$	Analytic $\mathcal{D}_n$	% Accuracy	$g_p(n'l'm_\pi)$
$1s\sigma_g$	$\sigma_g 1s$	-13.60569301	-13.60569301	$7.20(-9)$	$1/2$
$2p\sigma_u$	$\sigma_u 1s$	-13.60569301	-13.60569301	$7.20(-9)$	$1/2$
$2p\pi_u$	$\pi_u 2p$	-3.40142195	-3.40142325	$3.84(-5)$	$1/4$
$3p\sigma_u$	$\sigma_u 2s$, $\sigma_u 2p$	-3.40109672	-3.40142325	$9.60(-3)$	$1/4$, $1/8$
$3p\pi_u$	$\pi_u 3p$, $\pi_u 3d$	-1.51125386	-1.51174367	$3.24(-2)$	$1/7$, $1/9$
$4p\sigma_u$	$\sigma_u 3s$, $\sigma_u 3p$, $\sigma_u 3d$	-1.51076406	-1.51174367	$6.48(-2)$	$1/6$, $1/14$, $1/18$
$4f\sigma_u$	$\sigma_u 2s$, $\sigma_u 2p$	-3.40174979	-3.40142325	$9.60(-3)$	$1/4$, $1/8$
$4f\pi_u$	$\pi_u 3p$, $\pi_u 3d$	-1.51223347	-1.51174367	$3.24(-2)$	$1/7$, $1/9$
$4p\pi_u$	$\pi_u 4p$, $\pi_u 4d$, $\pi_u 4f$	-0.84250726	-0.85035581	$9.23(-1)$	$1/10$, $1/14$, $1/16$

Notes. The present asymptotic energies $\mathcal{D}_n$ are compared with the analytic values of the hydrogen atom and the percent accuracy is given. The number in parentheses indicates that the entry is multiplied by 10 to the power of that number.

coefficient is given by (Light et al. 1969)

$$
\begin{aligned}
\mathcal{R}(T; XY^+) &= \sqrt{\frac{8}{\mu\pi}}\left(\frac{1}{k_B T}\right)^{3/2} \\
&\times \int_0^\infty \sigma_{f,iE_{k_i}}^{RA}(E_{k_i}; XY^+)E_{k_i}e^{-E_{k_i}/k_B T}dE_{k_i} \\
&= 1.735(\mu T^3)^{-1/2}\int_0^\infty \sigma_{f,iE_{k_i}}^{RA}(E_{k_i}; XY^+) \\
&\times E_{k_i}e^{-E_{k_i}/k_B T}dE_{k_i} \quad \text{cm}^3\,\text{s}^{-1},
\end{aligned} \tag{29}
$$

where all the variables substituted into Equation (29) are in atomic units, T is in K, and we note that E_{k_i} is the initial (relative) kinetic energy.

3. Results

3.1. Calculation Details

The potential energy curves presented in Figure 1 are produced from a diagonalization procedure of the electronic Hamiltonian as described in Section 2.1. Here we chose to diagonalize the electronic Hamiltonian over an internuclear distance grid R, which is broken up into sections that had different internuclear distance spacing dR. For $0.05 \leqslant R \leqslant 14$, the internuclear distance spacing was $dR = 0.05$. For $14 < R \leqslant 50$, we used $dR = 2$, and for $50 < R \leqslant 200$, we utilized $dR = 15$, where $R_{max} = 200$. For $R > 200$, we assume the electronic dipole-matrix elements are constant with the values taken at $R_{max} = 200$, which is a reasonable approximation considering the extent of the bound $H_2^+(1s\sigma_g)$ vibrational wave functions. From $200 < R \leqslant 500$, we utilize the asymptotic potential energy curve forms of Sonnleitner et al. (1996) for the asymptotic H($n \leqslant 3$) states. For $500 < R \leqslant 600$, we assume that the [H(nl)+H$^+$]($n'l'm_\pi$) system has dissociated and take the dissociation energy as a constant value, which is taken at $R_{\mathcal{D}_n} = 500$. The integration of the electronic-vibrational dipole-matrix elements was from $0 < R \leqslant 600$.

The one-electron basis was constructed from a Hylleraas basis in combination with a spherical harmonics basis, which had a maximum value of orbital angular momentum $l_{max} = 60$. The one-electron orbital basis functions (Equation (49)) are constructed as such that the good quantum numbers (m, π, s) of the target states are satisfied, where the parity $\pi = (-1)^l$ and l are the orbital angular momentum. The Hylleraas basis

was constructed with $k_{max}(l) = 60 - l$ Hylleraas functions (Equation (50)) for $l \leq 20$ and $k_{max}(l) = 40$ functions for $20 < l \leq 60$ with $\alpha_m = 2.0$. Here only σ and π one-electron target states are required (due to the dipole selection rules of the electronic ground state), hence the Hylleraas basis and spherical harmonics basis have functions with orbital angular momentum projection m = 0 and $m = 1$. This one-electron basis was utilized across the entire range of $0 < R \leq 200$.

Referring to Figure 1, there are several electronic states of the same (m, π, s) symmetry that have potential energy curves that cross. Here we kept the nine energetically lowest electronic states per (m, π, s) symmetry for each R and then reordered the states in order to keep the $1s\sigma_g$, $2p\sigma_u$, $2p\pi_u$, $3p\sigma_u$, $3p\pi_u$, $4p\sigma_u$, $4f\sigma_u$, $4f\pi_u$, and $4p\pi_u$ states. We traced the electronic states by following the potential energy curves, electronic dipole-matrix elements, and mean radial electronic distance from the midpoint of the two nuclei $\langle r \rangle$.

Comparing our energies at $R_{max} = 200$ with the analytic potential energy curves given by Sonnleitner et al. (1996), we find that the potential energy curves are almost identical. In Table 2, we present the dissociation energies taken here. The inaccuracy of the $4p\pi_u$ dissociation energy is not associated with the convergence of the electronic structure calculation but is due to the dissociation energy being defined as the energy of the $4p\pi_u$ state taken at $R_{\mathcal{D}_{4p\pi_u}} = 200$.

The vibrational wave functions were calculated with a single-center Laguerre basis taken to convergence (Zammit et al. 2013, 2014, 2017a). The basis utilized $N_N = 250$ basis functions for $N \leqslant 36$ with exponential fall-offs chosen as $\alpha_N = 2.0$.

3.2. Energy Levels and Static Dipole Polarizabilities

The present rovibrational energy levels of $H_2^+(1s\sigma_g)$ are presented in Table 3 for selected N. We compare our energy levels with the energy levels of Babb (2015) for the $N = 0$ and $N = \tilde{N}$ states, where $\tilde{N}$ is the largest rotational quantum number presented by Babb (2015). In general, our energy levels agree to within ~ 0.05 cm^{-1} of Babb (2015). Comparing our energy levels with the adiabatic calculations of Hunter et al. (1974), our energy levels are within ~ 10 cm^{-1} for each respective level, where the largest difference is for high N levels. The full list of the present $1s\sigma_g$ rovibrational energy levels for H_2^+ will be available in the dipole-matrix element tables.

Table 3
The Total Energy ε_{nvN} of the $H_2^+(1s\sigma_g, v, N)$ States, Presented in Units of cm^{-1} with Respect to the Dissociation Limit (Taken to Be Zero) and Compared with the Energy Levels of Babb (2015) for the $N = 0$ and $N = \tilde{N}$ States, Where $\tilde{N}$ is the Largest Rotational Quantum Number Presented by Babb (2015)

	$\varepsilon_{nvN=0}$		$N_{\max}, \tilde{N}$		ε_{nvN} for $N = \tilde{N}$ of Babb (2015)	
v	Present	Babb (2015)	Present	Babb (2015)	Present	Babb (2015)
0	−21375.91	−21375.95	35	14	−15980.65	−15980.67
1	−19183.89	−19183.93	34	17	−12121.79	−12121.81
2	−17119.20	−17119.24	33	19	−9151.78	−9151.79
3	−15177.62	−15177.66	31	20	−7056.20	−7056.21
4	−13355.58	−13355.62	30	21	−5153.90	−5153.91
5	−11650.15	−11650.20	28	22	−3452.84	−3452.85
6	−10059.05	−10059.10	27	22	−2451.19	−2451.20
7	−8580.63	−8580.67	25	23	−1136.35	−1136.36
8	−7213.87	−7213.92	24	23	−438.04	−438.05
9	−5958.46	−5958.50	22	22	−196.06	−196.06
10	−4814.77	−4814.81	20	20	−272.96	−272.97
11	−3783.97	−3784.00	19	19	−62.74	−62.75
12	−2868.05	−2868.09	17	17	−98.07	−98.08
13	−2069.96	−2069.99	15	15	−102.78	−102.79
14	−1393.70	−1393.73	13	13	−83.13	−83.13
15	−844.45	−844.47	11	11	−48.20	−48.21
16	−428.67	−428.69	9	9	−10.79	−10.79
17	−153.67	−153.68	6	6	−17.48	−17.49
18	−23.41	−23.41	3	3	−5.66	−5.66
19	−0.71	−0.71	1	1	−0.20	−0.20

Note. The largest bound rotational quantum number $N_{\max}$ for each vibrational level v is also presented and matches the calculations of Stancil (1994a).

Here we obtain 423 $H_2^+(1s\sigma_g)$ bound rovibrational levels, which agrees with the calculations of Stancil (1994a, 1994b). We note that Babb (2015) presented dipole-matrix elements of the $2p\sigma_u$ state for only 337 rovibrational levels of $H_2^+(1s\sigma_g)$. The omitted rovibrational levels' dipole-matrix elements were considered too small for the table (J. Babb 2017, private communication). The data omitted by Babb (2015) are indicated in Table 3. The adiabatic calculations of Hunter et al. (1974) presented 421 bound rovibrational levels, which match the present bound levels except for the $v = 19$ bound states obtained here. Note that there is experimental evidence of bound $v = 19$, $N = 0, 1$ states (Carrington et al. 1989; Critchley et al. 2001).

The present partition functions are presented in Table 4 and compared with the results of Stancil (1994a, 1994b) for a range of material temperatures. In general, we are in good agreement with the calculations of Stancil (1994a, 1994b); however, the level of agreement decreases as the temperature increases. This discrepancy is puzzling. As indicated in Table 3, both calculations obtained the same number of bound rovibrational states of $H_2^+(1s\sigma_g)$. In addition, our energy levels are in good agreement with previous nonrelativistic Born–Oppenheimer (Babb 2015) and adiabatic (Hunter et al. 1974) calculations for the range of bound rovibrational levels available for comparison.

Utilizing the method described in Section 2.2 and Equation (15), we calculate the static dipole polarizability and the percentage contribution to the total static dipole polarizability from the electronic states $2p\sigma_u$, $2p\pi_u$, and the (electronic) continuum. The results are presented in Table 5 for H_2^+ in the bound $(1s\sigma_g, v_i, N_i = 0)$ states. The present total static dipole polarizabilities are in good agreement with the results of Bishop & Cheung (1979), which were calculated via approach (14) and are available up to $v_i = 10$. Here we give the percentage contribution of various channels in order to give an indication of which electronic excitation processes are expected

Table 4
The Partition Function of H_2^+ in the $1s\sigma_g$ State for a Range of Material Temperatures T_{mat} in Units of K

	$\mathcal{Q}_{XY^+}(T_{mat})$	
T_{mat} (K)	Present	Stancil (1994a)
1000	26.1	
2000	66.2	66.2
3150	142.1	142.1
5040	361.2	358.7
8400	1024.0	999.8
12600	2043.1	1968.2
16800	3009.2	2877.3
25200	4546.3	4313.8

to be important. Similarly, the oscillator strength sum rule could be used to determine which transitions are important.

3.3. Photodissociation

Here we present PD via excitation to the $2p\sigma_u$, $2p\pi_u$, $3p\sigma_u$, $3p\pi_u$, $4p\sigma_u$, $4f\sigma_u$, $4f\pi_u$, and $4p\pi_u$ states. For ease of comparison, we sum H_2^+ $n = 3$ ($3p\sigma_u$ and $3p\pi_u$), $n = 4$ ($4p\sigma_u$, $4f\sigma_u$, $4f\pi_u$, and $4p\pi_u$), and $n = 2, 3, 4$ excitations and represent them in the figures as $3p(\sigma_u + \pi_u)$, $4(p + f)(\sigma_u + \pi_u)$, and "Sum $n = 2, 3, 4$," respectively. The PD cross sections presented here are calculated via Equation (22).

We present in Figure 2 the PD cross section of H_2^+ in vibrationally excited states populated according to the BD weights (von Busch & Dunn 1972) and assuming $N_i = 0$. Here we compare our results with the calculations of Saha et al. (1980) and the only available measurements of von Busch & Dunn (1972). Above 110 nm, the PD cross section arises primarily from excitation to the $2p\sigma_u$ state. The present results are in good agreement with the experiment of von Busch & Dunn (1972) and are practically identical to the results of Saha et al. (1980). Below

Table 5
The Total $\alpha_{iv_iN_i}$, Parallel $\alpha^{\parallel}_{iv_iN_i}$, and Perpendicular $\alpha^{\perp}_{iv_iN_i}$ Static Dipole Polarizability of $H_2^+(1s\sigma_g, v_i, N_i = 0)$ and the Percent Contribution to the Total by the Electronic States $2p\sigma_u$, $2p\pi_u$, and the (Electronic) Continuum

| v_i | $\alpha_{iv_iN_i}$ | | $\alpha^{\parallel}_{iv_iN_i}$ | $\alpha^{\perp}_{iv_iN_i}$ | % Contribution to $\alpha_{iv_iN_i}$ | | |
	Present	Bishop & Cheung (1979)			$2p\sigma_u$	$2p\pi_u$	Continuum
0	3.17(0)	3.17(0)	5.83(0)	1.83(0)	61.22	33.51	1.72
1	3.89(0)	3.90(0)	7.69(0)	2.00(0)	65.56	29.83	1.49
2	4.82(0)	4.83(0)	1.01(1)	2.17(0)	69.71	26.26	1.29
3	6.01(0)	6.02(0)	1.33(1)	2.34(0)	73.66	22.83	1.11
4	7.56(0)	7.58(0)	1.76(1)	2.51(0)	77.38	19.55	0.96
5	9.62(0)	9.65(0)	2.35(1)	2.69(0)	80.87	16.47	0.83
6	1.24(1)	1.25(1)	3.15(1)	2.87(0)	84.08	13.62	0.71
7	1.63(1)	1.64(1)	4.28(1)	3.05(0)	87.02	11.02	0.61
8	2.18(1)	2.19(1)	5.90(1)	3.23(0)	89.65	8.70	0.51
9	3.00(1)	3.01(1)	8.31(1)	3.41(0)	91.96	6.66	0.42
10	4.24(1)	4.27(1)	1.20(2)	3.58(0)	93.96	4.92	0.34
11	6.23(1)	⋯	1.79(2)	3.75(0)	95.63	3.48	0.26
12	9.62(1)	⋯	2.81(2)	3.90(0)	97.00	2.32	0.19
13	1.59(2)	⋯	4.69(2)	4.05(0)	98.07	1.44	0.13
14	2.89(2)	⋯	8.58(2)	4.18(0)	98.88	0.80	0.08
15	6.09(2)	⋯	1.82(3)	4.30(0)	99.43	0.38	0.04
16	1.65(3)	⋯	4.95(3)	4.39(0)	99.78	0.14	0.02
17	7.70(3)	⋯	2.31(4)	4.45(0)	99.95	0.03	0.00
18	1.76(5)	⋯	5.29(5)	4.48(0)	100.00	0.00	0.00
19	1.54(7)	⋯	4.61(7)	4.49(0)	100.00	0.00	0.00

Notes. The total static dipole polarizabilities are compared with the results of Bishop & Cheung (1979), which are available up to $v_i = 10$. The number in parentheses indicates that the entry is multiplied by 10 to the power of that number.
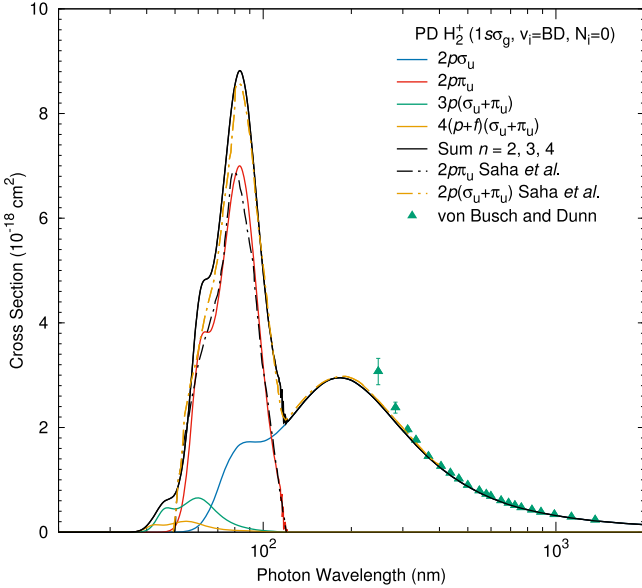

Figure 2. PD cross section of H_2^+ in vibrationally excited states, populated according to the von Busch & Dunn (1972) BD weights. The present results are for PD cross sections via excitation to the $2p\sigma_u$, $2p\pi_u$, $3p(\sigma_u + \pi_u)$, $4(p + f)(\sigma_u + \pi_u)$, and sum of $n = 2, 3, 4$ states; see the text for details. Results are compared with the calculations of Saha et al. (1980) and the measurements of von Busch & Dunn (1972).

110 nm, the $2p\pi_u$ state significantly contributes to the total PD cross section, and our PD cross section via the $2p\pi_u$ state is in good agreement with the calculations of Saha et al. (1980). At around 40–50 nm, the $n = 3$ and $n = 4$ PD cross sections are the major contributors to the total PD cross section.

In Figure 3, we present selected PD cross sections of H_2^+ from the $(1s\sigma_g, v_i = 4, N_i = 0)$, $(1s\sigma_g, v_i = 10, N_i = 0)$, and $(1s\sigma_g, v_i = 14, N_i = 0)$ states. Comparing the present $2p\sigma_u$

results with those of Babb (2015), we find excellent agreement. However, for highly excited vibrational states at low photon wavelengths, the calculations of Babb (2015) may not fully resolve the oscillatory structures found within the PD cross section. Depending on the initial state of the molecule, the PD threshold via the $2p\pi_u$ state is approximately in the 96–120 nm (10.2–12.9 eV) range, which for rovibrational excited initial states is very close to the position of the peak PD cross section. In the 96–120 nm region, the $2p\pi_u$ state PD cross section is generally one to two orders of magnitude larger than the $2p\sigma_u$ state PD cross section. In addition, the $2p\pi_u$ state cross section peak is generally two to three times larger than the magnitude of the $2p\sigma_u$ state cross section peak. The $2p\pi_u$ cross section dominates the total PD cross section at wavelengths below the $2p\pi_u$ PD threshold (approximately 96–120 nm), except at very low wavelengths, where it approaches zero and higher n-level cross sections contribute.

The $H_2^+(1s\sigma_g)$ LTE PD cross sections are presented in Figure 4 for selected material temperatures. We select material temperatures $T_{mat} = 3150, 5040, 8400, 12{,}600, 16{,}800$, and $25{,}200$ K and compare with the $2p\sigma_u$ results of Stancil (1994b), Lebedev & Presnyakov (2002), and Lebedev et al. (2003). Contrary to the level of agreement of the H_2^+ partition functions with Stancil (1994a, 1994b) at higher material temperatures (refer to Table 4), for the range of material temperatures considered, our $2p\sigma_u$ LTE PD cross sections are practically identical to the results of Stancil (1994b), Lebedev & Presnyakov (2002), and Lebedev et al. (2003). However, for the higher material temperatures, there is a minor discrepancy at the $2p\sigma_u$ cross section peak. The present results and the results of Lebedev & Presnyakov (2002) and Lebedev et al. (2003) agree with each other and are approximately 10% higher than the results of Stancil (1994b). The PD cross section via the $2p\pi_u$ state is the dominant contributor to the peak of the total
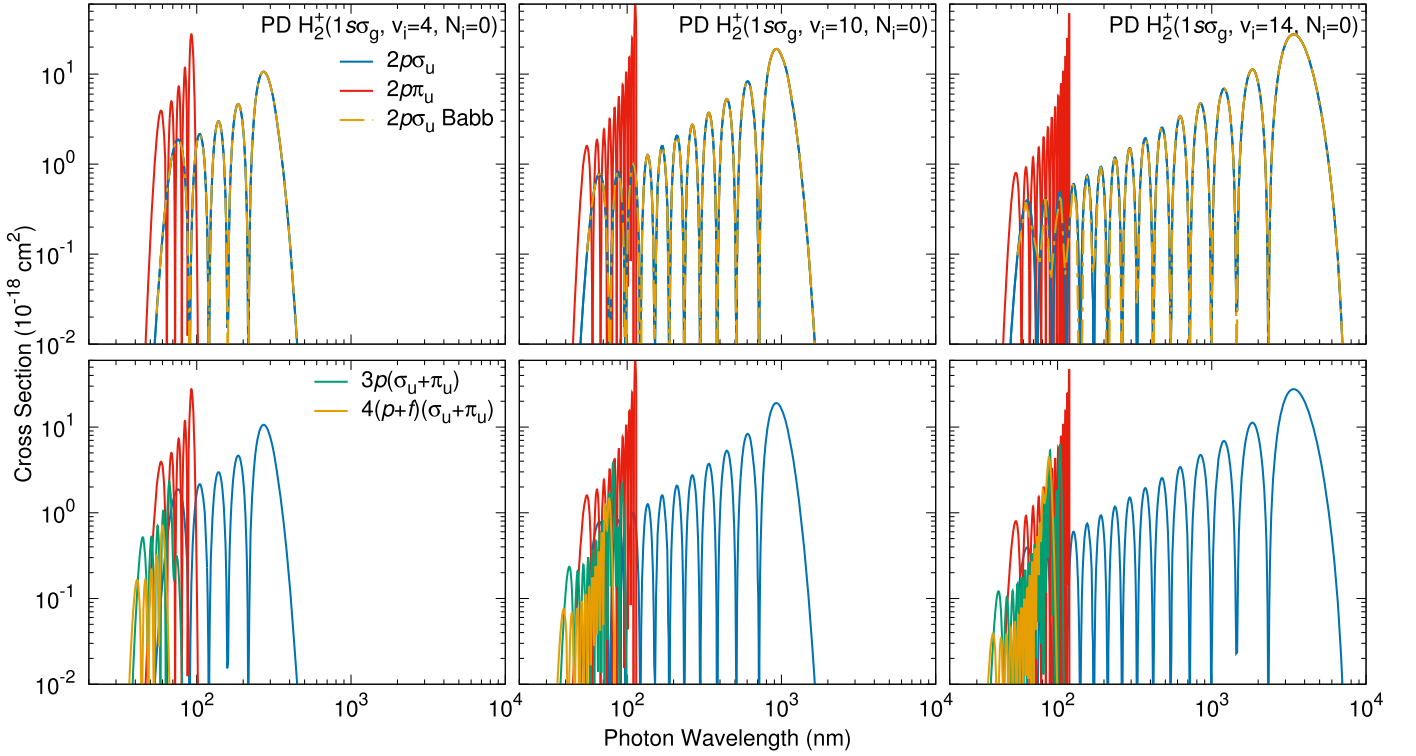
Figure 3. PD cross sections of H_2^+ in the $(1s\sigma_g, v_i = 4, N_i = 0)$, $(1s\sigma_g, v_i = 10, N_i = 0)$, and $(1s\sigma_g, v_i = 14, N_i = 0)$ states. PD cross sections are presented via excitation to the $2p\sigma_u$, $2p\pi_u$, $3p(\sigma_u + \pi_u)$, and $4(p + f)(\sigma_u + \pi_u)$ states; see the text for details. Present PD results via the $2p\sigma_u$ state are compared with the results of Babb (2015), which are practically identical above ~150 nm.

PD cross section, which is located (depending on the material temperature) below 120 nm. The $2p\pi_u$ PD cross section peak is approximately two to four times larger than the $2p\sigma_u$ PD cross section peak. The $n = 3$ and $n = 4$ PD cross sections noticeably contribute to the low-temperature total PD cross section at low wavelengths.

3.4. Radiative Association

Here we present RA results of $H_2^+(1s\sigma_g)$ via atomic hydrogen initially in the asymptotic H(1s) and H(2s) states (Equation (1)). Referring to Table 2, the asymptotic [H(1s)+H$^+$] state corresponds to the $1s\sigma_g$ or $2p\sigma_u$ potential energy curves of H_2^+, i.e., [H(1s)+H$^+$]($1s\sigma_g$) or [H(1s)+H$^+$]($2p\sigma_u$), respectively. The asymptotic [H(2s)+H$^+$] state corresponds to the H_2^+ potential energy curves $3p\sigma_u$, $4f\sigma_u$, $2s\sigma_g$, or $3d\sigma_g$. RA cross sections presented here are calculated via Equation (23) unless explicitly stated otherwise.

In Figure 5, we present the total RA cross sections of $H_2^+(1s\sigma_g)$. Comparing the present results with those of Stancil et al. (1993) for RA via the [H(1s)+H$^+$]($2p\sigma_u$) channel, we find very good agreement over the entire energy range. The resonance in the total RA cross section at ~1–2 × 10⁻⁴ eV is explained in detail by Stancil et al. (1993) and arises from a rotationally enhanced van der Waals well of the excited state. In our calculations, the resonance cross section comes primarily from the $N_i = 3$ partial wave, with RA into the $H_2^+(1s\sigma_g, v_f, N_f = 3)$ $v_f = 15$, 16, and 17 levels. It is worth noting that the individual final state contributions to the total resonance cross section do not agree with the results of Stancil et al. (1993). This is due to the use of the approximations given in Equations (9) and (10). However, the total $N_i = 3$ partial-wave contribution to the cross section agrees with the results of Stancil

et al. (1993). The validity of the approximations given in Equations (9) and (10) is investigated below.

Next, in Figure 5, we look at the RA cross section of $H_2^+(1s\sigma_g)$ from the individual dipole-transition components of the asymptotic [H(2s)+H$^+$] state, i.e., [H(2s)+H$^+$]($3p\sigma_u$) and [H(2s)+H$^+$]($4f\sigma_u$). It is worth noting that at low energies, the [H(2s)+H$^+$]($3p\sigma_u$) and [H(2s)+H$^+$]($4f\sigma_u$) RA cross sections are difficult to converge. We found that the cross sections are very sensitive to the separated atom energy $\mathcal{D}_n$, particularly for the [H(2s)+H$^+$]($3p\sigma_u$) channel, which has a repulsive interaction potential [$V_n(R)$ in Equation (4)]. Hence, at low energies, the [H(2s)+H$^+$]($3p\sigma_u$) RA cross section approaches zero. Convergence of the cross sections was checked by varying the extent of $R_{\mathcal{D}_n}$ (the potential energy curve value at R that we assigned $\mathcal{D}_n$). At near-zero E_{k_i}, the [H(2s)+H$^+$]($4f\sigma_u$) RA cross section is approximately four orders of magnitude larger than the RA cross section via the [H(1s)+H$^+$]($2p\sigma_u$) channel. Above 0.01 eV, the RA cross section via the [H(2s)+H$^+$]($3p\sigma_u$) channel is comparable to the [H(2s)+H$^+$]($4f\sigma_u$) cross section. RA via the [H(2s)+H$^+$]($4f\sigma_u$) channel is significantly larger than RA via the [H(1s)+H$^+$]($2p\sigma_u$) channel up to ~1 eV, where the cross sections become comparable. Above ~3 eV, the RA cross sections of the [H(2s)+H$^+$]($3p\sigma_u$) and [H(2s)+H$^+$]($4f\sigma_u$) channels decrease significantly. The significant difference in the RA cross section via excited-state (anti-)atoms, i.e., [$\bar{H}(2s)+\bar{H}^-$], could be utilized as an efficient mechanism for producing antimolecular hydrogen ions $\bar{H}_2^-$, which could then be used to grow antimatter clusters (M. Charlton 2017, private communication). We would expect higher excited states with an attractive interaction potential [$V_n(R)$ in Equation (4)] to have an even larger RA cross section at the low energies.

The state-resolved RA cross section and the approximate-sum RA cross section (Equation (19)), constructed utilizing the approximations summarized in Equations (9) and (10),
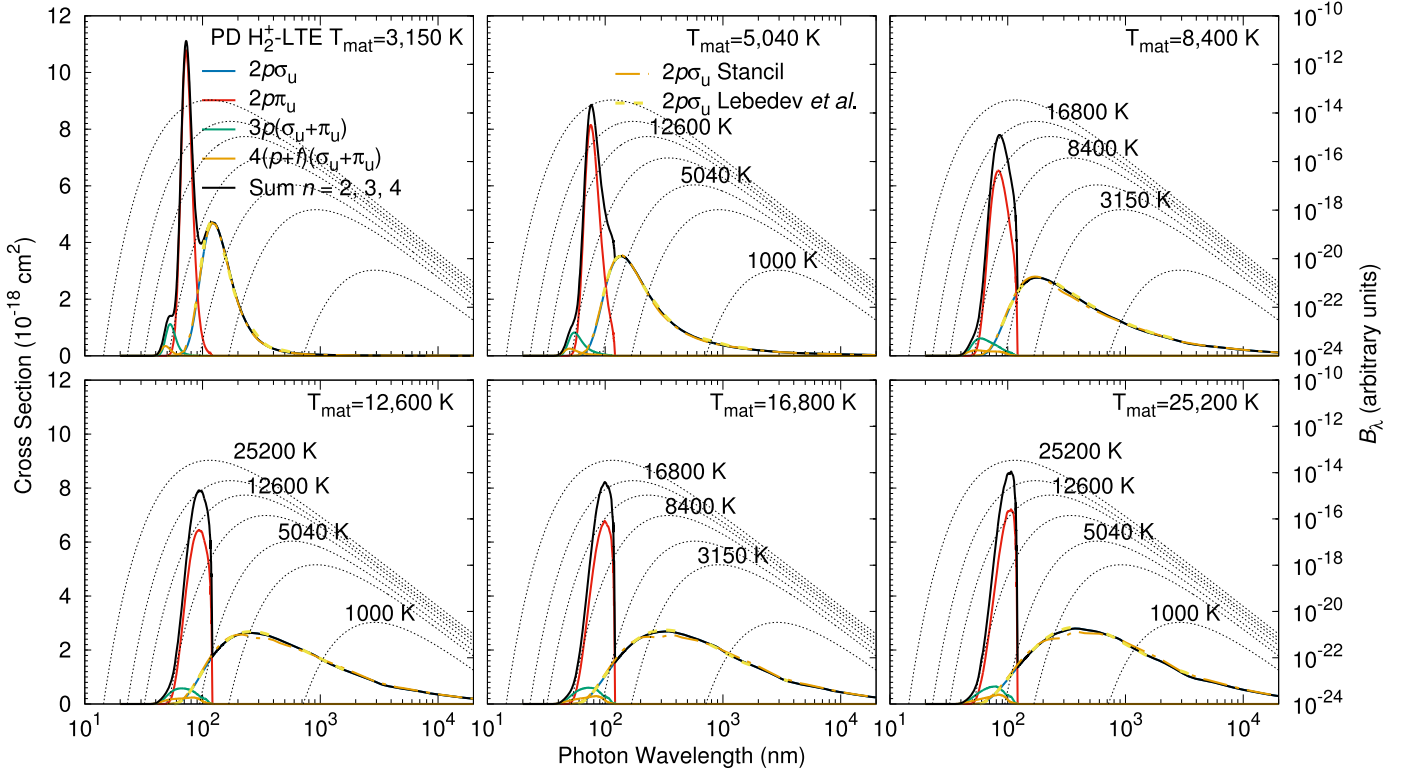
Figure 4. PD cross sections of H_2^+ assuming an LTE population of the rovibrationally excited states of the electronic ground state $1s\sigma_g$ at selected material temperatures, T_{mat}. PD cross sections are presented via excitation to the $2p\sigma_u$, $2p\pi_u$, $3p(\sigma_u + \pi_u)$, $4(p + f)(\sigma_u + \pi_u)$, and sum of $n = 2, 3, 4$ states; see the text for details. Present PD results via the $2p\sigma_u$ state are compared with the results of Stancil (1994b), Lebedev & Presnyakov (2002), and Lebedev et al. (2003), which are practically identical. The dotted lines are Planck distributions plotted as a function of photon wavelength, B_λ, at temperatures $T_{rad}= 1000, 3150, 5040, 8400, 12,600, 16,800$, and $25,200$ K.
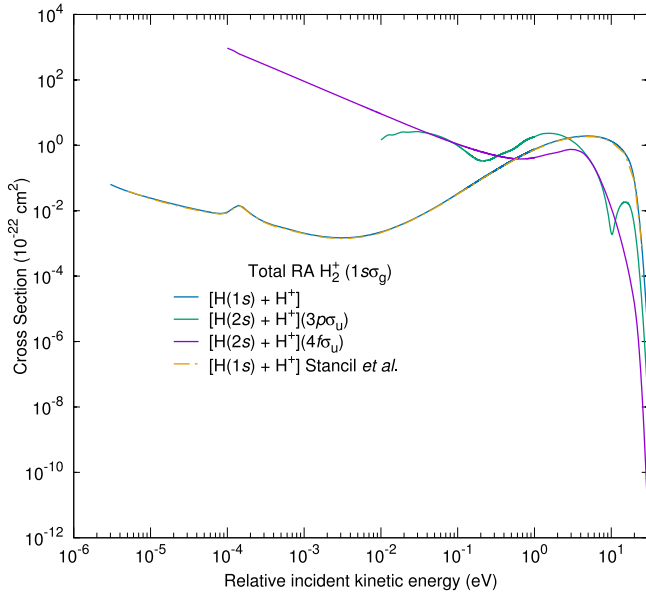
Figure 5. Total RA cross sections of $H_2^+(1s\sigma_g)$ via the $[H(2s)+H^+](3p\sigma_u)$ and $[H(2s)+H^+](4f\sigma_u)$ channels and the sum of the $[H(1s)+H^+]$ state. The present total RA cross section via the asymptotic $[H(1s)+H^+]$ state is compared with the results of Stancil et al. (1993), which are practically identical over the entire energy range.

Figure 6. RA cross section via the $2p\sigma_u$ channel into the $H_2^+(1s\sigma_g, v_f = 10, 14, 17, N_f = 2, 5)$ levels. The RA cross section is calculated utilizing the state-resolved cross section and the sum approximation from Equation (19), labeled as "Ap." in the figure.

are presented in Figure 6. Here we compare the RA cross sections via the $2p\sigma_u$ channel into the $H_2^+(1s\sigma_g, v_f = 10, 14, 17, N_f = 2, 5)$ levels. It is apparent that the
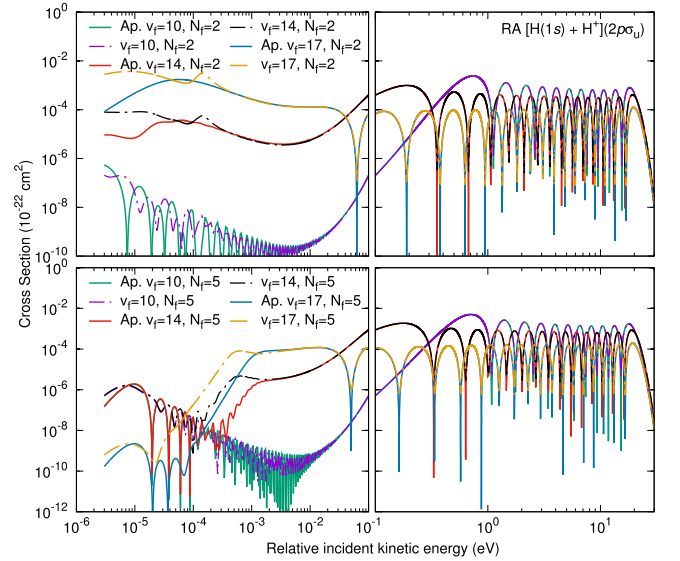
approximate-sum RA cross section (Equation (19)) does well for energies above $\sim 10^{-2}$ eV but significantly loses accuracy at energies below $\sim 10^{-3}$ eV. Note that the approximate total RA cross section (summed over all final states) is accurate to within $\sim 5\%$ across the entire energy range considered.
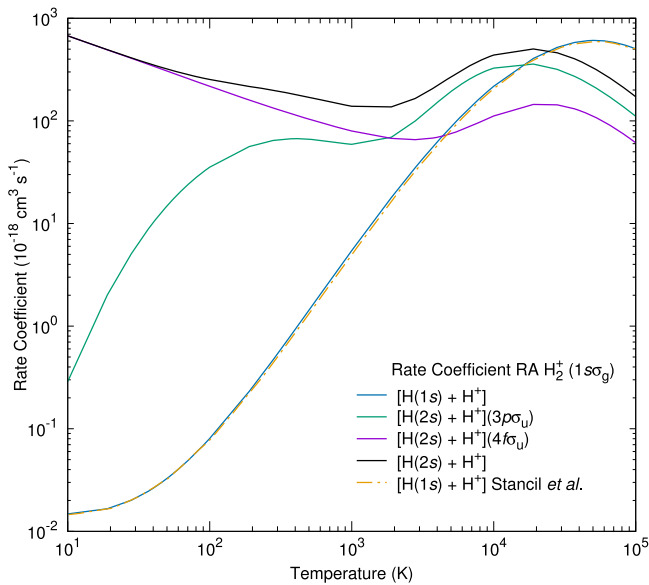
Figure 7. Rate coefficient for the total RA of $H_2^+(1s\sigma_g)$ as a function of the effective temperature. Here we present RA data via the $[H(2s)+H^+](3p\sigma_u)$ and $[H(2s)+H^+](4f\sigma_u)$ channels and the sum of the $[H(1s)+H^+]$ and $[H(2s)+H^+]$ states. The present rate coefficient for the total RA of $H_2^+(1s\sigma_g)$ via the asymptotic $[H(1s)+H^+]$ state is compared with the results of Stancil et al. (1993) and is practically identical over the entire temperature range.

The total RA cross sections are averaged over the Maxwellian distribution of the ion velocity and atom velocity as in Equation (29), and the rate coefficient for the RA of $H_2^+(1s\sigma_g)$ is presented in Figure 7 as a function of the effective temperature. The present results are compared with the results of Stancil et al. (1993) for RA via the asymptotic $[H(1s)+H^+]$ state and are practically identical over the entire temperature range. The $[H(2s)+H^+]$ RA rate coefficient is four to five orders of magnitude larger than the $[H(1s)+H^+]$ RA rate coefficient at 10 K. By 10^4 K, the rate coefficients via the $[H(2s)+H^+]$ and $[H(1s)+H^+]$ states become comparable. Although the difference in the RA rate coefficient is large below 10^4 K for these respective asymptotic states, for LTE plasmas at these temperatures, $H(2s)$ is not populated enough for this process to be significant. For example, at 10^4 K, the population in the $H(2s)$ excited state can be five or more orders of magnitude smaller than the population in the $H(1s)$ ground state. However, for non-LTE plasmas that have an electron temperature higher than the ion temperature, RA via the excited states could be an important process. As discussed above, the $[H(2s)+H^+](3p\sigma_u)$ RA cross section is difficult to converge for very low energies. Here we assign to the $[H(2s)+H^+](3p\sigma_u)$ rate coefficient an uncertainty of between 10% and 50% for temperatures $T < 50$ K, where the largest uncertainty is at the lowest temperatures.

4. Astrophysical Implications

A key species in the radiative "cool-down" process and collapse of primordial gas clouds is H_2. Several studies have investigated the formation of first- or second-generation Population III stars from the collapse of a primordial gas cloud exposed to UV radiation (Haiman et al. 1996; Susa & Kitayama 2000; Kitayama et al. 2001; Omukai 2001; Yoshida et al. 2003; Susa & Umemura 2006; Yoshida et al. 2007; O'Shea & Norman 2008; Sugimura et al. 2016). The formation, destruction, and cooling of H_2 under these conditions is not

trivial to model (Coppola et al. 2016). In addition to the destruction of H_2 by ionizing and Lyman–Werner radiation, the production and cooling of H_2 can also be aided by self-shielding and shielding by other species (Draine & Bertoldi 1996). The formation of H_2 is promoted in weakly photoionized media (Haiman et al. 1996) or by an enhanced ionization fraction in the post-shock gas (Mac Low & Shull 1986; Shapiro & Kang 1987; Kang & Shapiro 1992; Koyama & Inutsuka 2000; Coppola et al. 2016). This promotion of H_2 formation occurs because cooling proceeds faster than recombination, leaving an enhanced ionization fraction of the H_2 intermediaries H^-, H_2^+, and H^+ (Coppola et al. 2016). The H_2^+ molecule plays an important role in the production of H_2 via the charge-exchange process:

$$H_2^+ + H \rightarrow H_2 + H^+. \qquad (30)$$
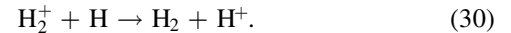
The calculations of Sugimura et al. (2016) suggest that this is the dominant H_2 production mechanism in primordial gas clouds immersed in radiation fields with $T_{rad} < 7000$ K. It should be noted that the calculations of Sugimura et al. (2016) utilized the correct H_2^+ RA cross-section formula (K. Sugimura 2017, private communication) from Babb (2015; Equation (7)) and showed a significant difference between LTE and non-LTE results.

The above physics is also relevant to several other astrophysical systems. For example, the Crab Nebula has bright H_2-emitting knots (Loh et al. 2010, 2011) that are exposed to a harsh environment of high-energy photons and particles (Hester 2008; Richardson et al. 2013). The synchrotron continuum radiation penetrates successive layers of the cloud where the outer ionized regions attenuate the incident radiation, allowing H_2 to form. Preliminary simulations (that did not include H_2^+ species) of Knot-51 with the CLOUDY code (Richardson et al. 2013) suggest that H_2 production was enhanced by a high electron density in the presence of H, which forms significant amounts of H^-. It would be interesting to investigate H_2 production via the H_2^+ channel (Equation (30)) in this system and see if conclusions similar to those of Sugimura et al. (2016) are reached. In addition, the Crab Nebula knots appear to be well-resolved prototypes of the much larger filaments seen in the intergalactic medium of cool-core galaxy clusters (Fabian et al. 2008; Richardson et al. 2013). Both show a low-ionization spectrum, have similar geometries, and are surrounded by ionizing particles (Richardson et al. 2013).

Bertoldi & Draine (1996) proposed that when molecular clouds are exposed to hot-stars radiation possessing photons with wavelengths less than 111 nm (such as the M17 northern bar and the Orion A M42), H_2^+ may be populated enough in the merged ionization and dissociation fronts to have detectable levels of rovibrational emission. They proposed that the H_2^+ population may even be high enough to react significantly with H_2 to produce H_3^+, which may also have detectable levels of rovibrational emission.

Although the total $2p\pi_u$ LTE PD cross section is two to six times larger than the $2p\sigma_u$ channel, this cross section is not likely to contribute significantly to the overall opacity of cool, hydrogen-rich DA white dwarf atmospheres (refer to Stancil 1994b; see Figure 6). This is primarily due to the very low abundance of H_2^+ in these environments and the overlapping H_2 ($X \rightarrow B, C$) and $H(1s \rightarrow 2p)$ absorption processes (and line wings). However, the H_2^+ $2p\pi_u$ PD channel may cause some "apparent" (although probably negligible) line broadening of the $H(1s \rightarrow 2p)$ line.

In models of the above systems, the present H_2^+ data may play an important role in the following physics.

(1) The PD of H_2^+ via UV photons and, consequently, the decreased rate of the H_2 charge-exchange production mechanism (Equation (30)) is likely to be important in the dissociation regions of molecular clouds (Bertoldi & Draine 1996; Draine & Bertoldi 1996).

(2) The enhanced H_2^+ RA cross section via the [H(2s)+H$^+$] state may be significant at the merged ionization and dissociation shock front (Bertoldi & Draine 1996). This may enhance the production of H_2^+ and, consequently, H_2.

In addition to points (1) and (2), the overall chemistry and cooling of the gas will also be influenced by electron scattering from H_2^+ and H_2. Recently, we provided (Pitchford et al. 2016) the first demonstratively convergent (accurate to ~5%–15%, depending on the transition) state-resolved e^-–$H_2^+(1\sigma_g, v_i = 0 - 9)$ (Zammit et al. 2014) and e^-–$H_2(X^1\Sigma_g^+, v_i = 0)$ (Zammit et al. 2016, 2017b) scattering data over a broad range of impact energies, which includes excitation and ionization processes. Of particular importance to the H_2 chemistry network is the electron-impact dissociation process of H_2, which we have shown is lower than recommended cross sections by a factor of two (Zammit et al. 2017b).

5. Conclusion

We have presented state-resolved cross sections for PD and RA of $H_2^+(1s\sigma_g)$ via the first eight dipole-allowed electronic states, i.e., $2p\sigma_u$, $2p\pi_u$, $3p\sigma_u$, $3p\pi_u$, $4p\sigma_u$, $4f\sigma_u$, $4f\pi_u$, and $4p\pi_u$. The results are in excellent agreement with previous theoretical studies and experiments.

We found a major enhancement of the total PD cross section at wavelengths around 100 nm, which is attributed to transitions to the $2p\pi_u$ state. The RA cross section via the [H(2s)+H$^+$] reaction channel was found to be four to five orders of magnitude larger than that via the [H(1s)+H$^+$] channel at low energies. This process could be an efficient mechanism for producing antimolecular hydrogen ions $\bar{H}_2^-$, which could then be used to grow antimatter clusters (M. Charlton 2017, private communication).

We discussed possible astrophysical implications of this data, which are likely to impact the physics of H_2 formation (Equation (30)) in molecular gas clouds under UV-accessible radiation. These conditions are found in molecular gas cloud candidates for Population III star formation, the Crab Nebula filaments, and the filaments seen in the intergalactic medium of cool-core galaxy clusters.

Tables of the dipole-matrix elements and energies needed to calculate comprehensive state-resolved cross sections and rate coefficients will be made publicly available for transitions between the ground electronic state $1s\sigma_g$ and the $2p\sigma_u$, $2p\pi_u$, $3p\sigma_u$, $3p\pi_u$, $4p\sigma_u$, $4f\sigma_u$, $4f\pi_u$, and $4p\pi_u$ electronic states.

Appendix
Molecular States

The target molecule Hamiltonian H_T in the laboratory frame of reference is given as

$$H_T = -\frac{1}{2}\sum_{j=1}^{N_e}\nabla_j^2 - \sum_{j=1}^{N_e}\sum_{i=1}^{N_n}\frac{Z_i}{|\mathbf{r}_j - \mathbf{R}_i|} + \sum_{i>j=1}^{N_e}\frac{1}{|\mathbf{r}_j - \mathbf{r}_i|}$$
$$-\sum_{i=1}^{N_n}\frac{1}{2M_i}\nabla_i^2 + \sum_{j>i=1}^{N_n}\frac{Z_iZ_j}{|\mathbf{R}_i - \mathbf{R}_j|}, \quad (31)$$

where the target molecule has N_e electrons, N_n nuclei with charge Z, and mass M. Referring to Section 2.1, the molecular states $\bar{\Phi}_{nvNm_N}(\mathbf{x}, \mathbf{R})$ are formulated within the nonrelativistic Born–Oppenheimer approximation

$$\bar{\Phi}_{nvNm_N}(\mathbf{x}, \mathbf{R}) \approx \Phi_n(\mathbf{x}; \mathbf{R})\nu_{nvN}(R)R_{nNm_N}(\hat{\mathbf{R}}). \quad (32)$$

In the body (molecular fixed) frame of reference, the H_2^+ target electronic Hamiltonian H_T^{elec} in the Born–Oppenheimer approximation describes an electron in the Coulomb potential of two protons that are fixed at a distance R and is defined as

$$H_T^{elec} = H_1^{elec} + 1/R, \quad (33)$$

where $1/R$ is the internuclear Coulomb repulsion term.

A.1. Separation of One-electron Electronic Schrödinger Equation in Spheroidal Coordinates

In the modified prolate-spheroidal coordinate system used here, we choose to have $\rho = \frac{R}{2}(\xi - 1)$ so that the modified coordinate system is defined as

$$\rho = \frac{r_1 + r_2}{2} - \frac{R}{2} \in [0, \infty), \quad \phi \in [0, 2\pi),$$
$$\eta = \frac{r_1 - r_2}{R} \in [-1, 1), \quad (34)$$

where r_1 and r_2 refer to the electron position from nuclei 1 and 2, respectively. With this choice of coordinate system, the integration volume element is

$$d\boldsymbol{\rho} = [(\rho + R/2)^2 - (\eta R/2)^2]d\rho d\eta d\phi, \quad (35)$$

where $\boldsymbol{\rho}$ collectively represents the (ρ, η, ϕ) coordinates. For a diatomic molecule formulated in the modified prolate-spheroidal coordinate system, the one-electron electronic Hamiltonian H_j^{elec} in the body frame of reference is given by

$$H_j^{elec} = K_j + V_j, \quad (36)$$

$$K = -\frac{1}{2}\frac{1}{\left(\rho + \frac{R}{2}\right)^2 - \left(\frac{R}{2}\eta\right)^2}\left\{\frac{\partial}{\partial\rho}\left[\rho(\rho + R)\frac{\partial}{\partial\rho}\right]\right.$$
$$\left. + \frac{\partial}{\partial\eta}\left[(1 - \eta^2)\frac{\partial}{\partial\eta}\right] + \left[\frac{R^2/4}{\rho(\rho + R)} + \frac{1}{1 - \eta^2}\right]\frac{\partial^2}{\partial\phi^2}\right\},$$
$$(37)$$

$$V = -\frac{1}{2}\frac{1}{\left(\rho + \frac{R}{2}\right)^2 - \left(\frac{R}{2}\eta\right)^2}\{-Z_+(2\rho + R) + Z_-R\eta\}, \quad (38)$$

where K is the kinetic energy operator, V is the electron-nuclei Coulomb potential, $Z_\pm = z_j(Z_1 \pm Z_2)$, and the charge of the

electron $z_j = -1$. Substituting the above Hamiltonian Equation (36) into the one-electron electronic Schrödinger equation $(E - H^{elec})|\Phi\rangle = 0$ and multiplying through by $2\left[\left(\rho + \frac{R}{2}\right)^2 - \left(\frac{R}{2}\eta\right)^2\right]$, we obtain

$$\left\{ 2\left[\left(\rho + \frac{R}{2}\right)^2 - \left(\frac{R}{2}\eta\right)^2\right]E \right.$$
$$+ \frac{\partial}{\partial\rho}\left[\rho(\rho + R)\frac{\partial}{\partial\rho}\right] + \frac{\partial}{\partial\eta}\left[(1 - \eta^2)\frac{\partial}{\partial\eta}\right]$$
$$+ \left[\frac{R^2/4}{\rho(\rho + R)} + \frac{1}{1 - \eta^2}\right]\frac{\partial^2}{\partial\phi^2}$$
$$\left. - Z_+(2\rho + R) + Z_-R\eta\right\}\Phi(\boldsymbol{\rho}) = 0. \quad (39)$$

If we consider $\Phi(\boldsymbol{\rho})$ as separable and assume the same ϕ-dependence as the spherical harmonics, it can be expressed as

$$\Phi(\boldsymbol{\rho}) = \Xi(\rho)\Upsilon(\hat{\boldsymbol{\rho}}), \quad (40)$$

where the spheroidal harmonics $\Upsilon(\hat{\boldsymbol{\rho}}) = H(\eta)\exp(im\phi)$ and $\hat{\boldsymbol{\rho}} \equiv (\cos^{-1}(\eta), \phi)$. Substituting Equation (40) into the Schrödinger Equation (39), it becomes

$$\left\{ 2\left(\rho + \frac{R}{2}\right)^2 E + \frac{\partial}{\partial\rho}\left[\rho(\rho + R)\frac{\partial}{\partial\rho}\right] \right.$$
$$- \frac{m^2R^2/4}{\rho(\rho + R)} - Z_+(2\rho + R)$$
$$- 2\left(\frac{R}{2}\eta\right)^2 E + \frac{\partial}{\partial\eta}\left[(1 - \eta^2)\frac{\partial}{\partial\eta}\right]$$
$$\left. - \frac{m^2}{1 - \eta^2} + Z_-R\eta\right\}\Xi(\rho)\Upsilon(\hat{\boldsymbol{\rho}}) = 0, \quad (41)$$

noting that $\frac{\partial^2}{\partial\phi^2}\Upsilon(\hat{\boldsymbol{\rho}}) = -m^2\Upsilon(\hat{\boldsymbol{\rho}})$. Dividing the above equation by Equation (40), we obtain

$$\frac{1}{\Xi(\rho)}\left\{ 2\left(\rho + \frac{R}{2}\right)^2 E + \frac{\partial}{\partial\rho}\left[\rho(\rho + R)\frac{\partial}{\partial\rho}\right] \right.$$
$$\left. - \frac{m^2R^2/4}{\rho(\rho + R)} - Z_+(2\rho + R)\right\}\Xi(\rho)$$
$$+ \frac{1}{\Upsilon(\hat{\boldsymbol{\rho}})}\left\{ -2\left(\frac{R}{2}\eta\right)^2 E + \frac{\partial}{\partial\eta}\left[(1 - \eta^2)\frac{\partial}{\partial\eta}\right] \right.$$
$$\left. - \frac{m^2}{1 - \eta^2} + Z_-R\eta\right\}\Upsilon(\hat{\boldsymbol{\rho}}) = 0. \quad (42)$$

In order for Equation (42) to be true for any value of ρ and η, the expressions within the two braces must each be a constant of equal magnitude but opposite sign. This constant is known as the separation constant A. Hence, we can now separate the Schrödinger Equation (42) into a "radial" equation,

$$\left\{ 2\left(\rho + \frac{R}{2}\right)^2 E + \frac{\partial}{\partial\rho}\left[\rho(\rho + R)\frac{\partial}{\partial\rho}\right] \right.$$
$$\left. - \frac{m^2R^2/4}{\rho(\rho + R)} - Z_+(2\rho + R) - A\right\}\Xi(\rho) = 0, \quad (43)$$

and an "angular" equation,

$$\left\{ -2\left(\frac{R}{2}\eta\right)^2 E + \frac{\partial}{\partial\eta}\left[(1 - \eta^2)\frac{\partial}{\partial\eta}\right] \right.$$
$$\left. - \frac{m^2}{1 - \eta^2} + Z_-R\eta + A\right\}\Upsilon(\hat{\boldsymbol{\rho}}) = 0, \quad (44)$$

that are connected by the constant A. It is important to note that as the nuclei separation $R \to 0$, the above Schrödinger equations should approach the united atom limit Schrödinger equation formulated in spherical coordinates. Substituting $\eta = \cos(\theta)$ for $R = 0$ into the "angular" Equation (44), we obtain the Laplace angular equation

$$\left\{ \frac{1}{\sin(\theta)}\frac{\partial}{\partial\theta}\left[\sin(\theta)\frac{\partial}{\partial\theta}\right] - \frac{m^2}{\sin^2(\theta)} + A\right\}\Upsilon(\hat{\boldsymbol{\rho}}) = 0, \quad (45)$$

where the separation constant becomes $A = l(l + 1)$ and $\Upsilon(\hat{\boldsymbol{\rho}}) = Y_{lm}(\theta, \phi)$. To preserve this limiting behavior, we expand the spheroidal harmonics on the basis of spherical harmonics,

$$\Upsilon(\hat{\boldsymbol{\rho}}) = \sum_l d_l Y_{lm}(\hat{\boldsymbol{\rho}}), \quad (46)$$

where d_l are expansion coefficients.

A.2. Electronic Wave Functions

The electronic target states of H_2^+ are characterized by the projection of orbital angular momentum m, parity π, and spin s, with $s = 1/2$. Here we suppress the explicit dependence on the internuclear separation R. For each combination of (m, π, s), the generalized eigenvalue problem (for either an orthogonal or a nonorthogonal basis $\{\phi_i\}$),

$$\sum_{j=1}^N (\langle\phi_i|H_T^{elec}|\phi_j\rangle - \varepsilon^{elec}(R)\langle\phi_i|\phi_j\rangle)C_j = 0, \quad (47)$$

is solved via diagonalization of the target electronic Hamiltonian (Equation (33)) to obtain energies $\varepsilon^{elec}(R)$ (eigenvalues) and expansion coefficients C_j (eigenvectors). This is done for each internuclear separation R. We represent the one-electron wave functions as an expansion over one-electron orbitals,

$$\Phi_n^{m\pi}(\boldsymbol{x}) = \sum_{\gamma=1}^{\mathcal{N}} C_\gamma^{(n)}\phi_\gamma^{m\pi}(\boldsymbol{x}), \quad (48)$$

where $\boldsymbol{x}$ denotes the electronic spin and spatial coordinates and $\mathcal{N}$ is the total number of one-electron orbitals $\phi_j^{m\pi}(\boldsymbol{x})$. One-electron orbitals are represented by

$$\phi_\gamma^{m\pi}(\boldsymbol{x}) = \varphi_{k_\gamma m_\gamma}(\rho)Y_{l_\gamma m_\gamma}(\hat{\boldsymbol{\rho}})\chi_{m_{s_\gamma}}(\sigma), \quad (49)$$

with $m = m_\gamma$ and $(-1)^{l_\gamma} = \pi$, and $\chi_{m_{s_\gamma}}(\sigma)$ is the spin-$\frac{1}{2}$ eigenfunction with angular projection m_{s_γ}. The Hylleraas functions are defined as

$$\varphi_{km}(\rho) = \sqrt{\frac{\alpha_m(k - 1)!}{(k + m - 1)!}}$$
$$\times (\alpha_m\rho)^{m/2}\exp(-\alpha_m\rho/2)L_{k-1}^m(\alpha_m\rho), \quad (50)$$

where α_m is the exponential fall-off parameter, L_{k-1}^m are the associated Laguerre polynomials of order m, and k ranges from

Table 6
Components of the Dipole-length Operator Acting on an Electron in Cartesian, Spherical, and Prolate-spheroidal Coordinates and the Atomic (*LS*-coupling) Selection Rules of the Operator (Assuming $s_f = s_i$), Where f and i Indicate Final and Initial States, Respectively

Polarization	Cartesian	Spherical	Prolate-spheroidal	Selection Rules for Atomic States
Linear	z	$\sqrt{\frac{4\pi}{3}}\,rY_{1,0}(\theta,\phi)$	$\sqrt{\frac{4\pi}{3}}\,(\rho+R/2)Y_{1,0}(\eta,\phi)$	$l_f = l_i \pm 1,\ m_f = m_i$
Circular C	$-\frac{1}{\sqrt{2}}(x+iy)$	$\sqrt{\frac{4\pi}{3}}\,rY_{1,1}(\theta,\phi)$	$\sqrt{\frac{4\pi}{3}}\,\sqrt{\rho(\rho+R)}\,Y_{1,1}(\eta,\phi)$	$l_f = l_i \pm 1,\ m_f = m_i + 1$
Circular CC	$\frac{1}{\sqrt{2}}(x-iy)$	$\sqrt{\frac{4\pi}{3}}\,rY_{1,-1}(\theta,\phi)$	$\sqrt{\frac{4\pi}{3}}\,\sqrt{\rho(\rho+R)}\,Y_{1,-1}(\eta,\phi)$	$l_f = l_i \pm 1,\ m_f = m_i - 1$

Note. The light is polarized linearly parallel to the z-axis, circularly polarized clockwise (C) in the x, y-plane, or circularly polarized counterclockwise (CC) in the x, y-plane.

1 to $k_{\max}$ (l) for each value of l. The largest value of orbital angular momentum in the one-electron basis is $l_{\max}$ (here $l_{\max} = 60$) Note that spherical harmonics are used in the one-electron basis (Equation (49)) because they are used as a basis to construct the spheroidal harmonics (Equation (46)). With this one-electron orbital basis (Equation (49)), the one-electron Hamiltonian matrix elements in Equation (47) are primarily evaluated analytically. For convenience, we express the electronic target states as

$$\Phi_n^{m\pi}(\boldsymbol{\rho}) = \sum_{kl} C_{kl}^{(n)} \varphi_{km}(\rho) Y_{lm}(\hat{\boldsymbol{\rho}})$$
$$= \sum_{l} X_l^{(n)}(\rho) Y_{lm}(\hat{\boldsymbol{\rho}}), \qquad (51)$$

where

$$X_l^{(n)}(\rho) = \sum_{k} C_{kl}^{(n)} \varphi_{km}(\rho). \qquad (52)$$

By performing structure calculations over the range of R and interpolating, the Born–Oppenheimer potential energy curves $\varepsilon_n^{\mathrm{elec}}(R)$ are obtained (as defined by Bishop & Cheung 1977).

A.3. Vibrational Wave Functions

For a diatomic molecule in an electronic state n, the nonrelativistic Born–Oppenheimer Hamiltonian for the vibrational motion is given by Beckel et al. (1973):

$$H_n^{\mathrm{BO}} = -\frac{1}{2\mu}\frac{d^2}{dR^2} + \frac{N(N+1)-m_n^2}{2\mu R^2} + \varepsilon_n^{\mathrm{elec}}(R). \qquad (53)$$

It is important to note that states only exist for $N \geqslant m_n$ (Brown & Carrington 2003). Bound vibrational wave functions $\nu_{nvN}(R)$ are obtained via a diagonalization procedure of the vibrational Hamiltonian (Equation (53)) for each N using a set of nuclear orbitals

$$\xi_j(R) = \frac{1}{R}\varphi_{k_j N_j}(R). \qquad (54)$$

Here $\varphi_{k_j N_j}(R)$ are Laguerre basis functions, which are described in detail in Zammit et al. (2013, 2014, 2017a). We diagonalize the Hamiltonian (Equation (53)) with a large set of nuclear orbitals that is taken to convergence.

A.4. Dipole-matrix Elements

The dipole-length operator form for a photon interacting with an electron is given in Table 6. Generally, in photon-absorption processes, the photon is polarized in the laboratory (lab) frame (also known as the space-fixed frame) of reference,

where the photon can be polarized linearly parallel to the z-axis, circularly polarized clockwise in the x, y-plane, or circularly polarized counterclockwise in the x, y-plane.

To calculate electronic dipole-matrix elements, we transform the dipole-length operator from the lab frame to the body frame (also known as the molecule-fixed frame) of reference. Note that the electronic wave functions are formulated in the body frame of reference. Equations formulated in the lab and body frames are labeled by superscripts $^{\mathrm{(lab)}}$ and $^{\mathrm{(b)}}$, respectively. In spherical coordinates, the dipole-length operator in the lab frame of reference has the form

$$\mathcal{V}_\mu(\boldsymbol{r}^{(\mathrm{lab})}) = \sqrt{\frac{4\pi}{3}}\,rY_{1,\mu}(\boldsymbol{r}^{(\mathrm{lab})}), \qquad (55)$$

where μ indicates the photon polarization direction in the lab frame. We note the rotation definition

$$Y_{l,m}(\theta',\phi') = \sum_{\kappa} D_{\kappa,m}^l(\hat{\boldsymbol{\beta}}) Y_{l,\kappa}(\theta,\phi), \qquad (56)$$

where, in this operation, (θ,ϕ) are the space-fixed coordinates that are being rotated by the Wigner-D rotation matrices $D_{\kappa,m}^l(\hat{\boldsymbol{\beta}})$ Euler angles $\hat{\boldsymbol{\beta}}$ to produce (θ',ϕ') (Varshalovich et al. 1988). Here we only need to utilize two of the Euler angles to rotate our coordinate system to the body frame such that $\hat{\boldsymbol{\beta}} = (\phi_{\hat{\boldsymbol{R}}},\theta_{\hat{\boldsymbol{R}}},0) \equiv \hat{\boldsymbol{R}}^{(\mathrm{lab})}$, the orientation of the internuclear axis in the lab frame (Morrison & Sun 1995; Brown & Carrington 2003). The inverse rotation operation is given by Varshalovich et al. (1988):

$$Y_{l,m}(\theta,\phi) = \sum_{\kappa} D_{m,\kappa}^{l*}(\hat{\boldsymbol{\beta}}) Y_{l,\kappa}(\theta',\phi'), \qquad (57)$$

which can be shown noting that $D_{m,\kappa}^{l*}(\alpha,\beta,\gamma) = D_{\kappa,m}^l(-\gamma,-\beta,-\alpha)$. Utilizing the above definition (Equation (57)), the dipole-length operator can be transformed from the lab frame (Equation (55)) to the body frame and has the form

$$\mathcal{V}_\mu(\boldsymbol{r}^{(\mathrm{b})},\hat{\boldsymbol{R}}^{(\mathrm{lab})}) = \sqrt{\frac{4\pi}{3}}\,r\sum_{\kappa} D_{\mu,\kappa}^{1*}(\hat{\boldsymbol{R}}^{(\mathrm{lab})}) Y_{1,\kappa}(\hat{\boldsymbol{r}}^{(\mathrm{b})}). \qquad (58)$$

It is very important to note that with this frame transformation, κ now determines the transitions that are possible (not μ). The Wigner-D function in the operator (Equation (58)) is factored out of the electronic dipole-matrix element calculation and included in the calculation of the Hönl–London factors. Hence, for convenience, we express the dipole-length operator (Equation (58)) as

$$\mathcal{V}_\mu(\boldsymbol{r}^{(b)}, \hat{\boldsymbol{R}}^{(lab)}) = \sum_\kappa V_\kappa(\boldsymbol{r}^{(b)}) D^{1*}_{\mu,\kappa}(\hat{\boldsymbol{R}}^{(lab)}), \tag{59}$$

where $V_\kappa(\boldsymbol{r}^{(b)})$ is the dipole-length operator acting on the body-frame electronic wave function. Referring to Table 6, $V_\kappa(\boldsymbol{r}^{(b)})$ in Equation (59) can be formulated in spheroidal coordinates (in the body frame),

$$V_\kappa(\boldsymbol{r}^{(b)}) = \sqrt{\frac{4\pi}{3}} \, r \begin{cases} Y_{1,0}(\hat{\boldsymbol{r}}^{(b)}), & \kappa = 0, \quad m_f = m_i \\ Y_{1,\pm1}(\hat{\boldsymbol{r}}^{(b)}), & \kappa = \pm 1, \; m_f = m_i \pm 1 \end{cases}$$

$$= \sqrt{\frac{4\pi}{3}} \begin{cases} (\rho + R/2) Y_{1,0}(\hat{\boldsymbol{\rho}}), & \kappa = 0, \quad m_f = m_i \\ \sqrt{\rho(\rho + R)} \, Y_{1,\pm1}(\hat{\boldsymbol{\rho}}), & \kappa = \pm 1, \; m_f = m_i \pm 1 \end{cases}$$

$$= \mathcal{P}_\kappa(\rho) \begin{cases} Y_{1,0}(\hat{\boldsymbol{\rho}}), & \kappa = 0, \quad m_f = m_i \\ Y_{1,\pm1}(\hat{\boldsymbol{\rho}}), & \kappa = \pm 1, \; m_f = m_i \pm 1 \end{cases}, \tag{60}$$

where

$$\mathcal{P}_\kappa(\rho) = \sqrt{\frac{4\pi}{3}} \begin{cases} (\rho + R/2), & \kappa = 0 \\ \sqrt{\rho(\rho + R)}, & \kappa = \pm 1 \end{cases}. \tag{61}$$

The electronic dipole-matrix elements $\mathcal{M}_{f,i}(R) = \langle \Phi_f | V_\kappa | \Phi_i \rangle_{\boldsymbol{r}^{(b)}}$ in Equation (8) can be evaluated analytically for the spheroidal "angular terms" $\hat{\boldsymbol{\rho}}$, where $\langle \Phi_f | V_\kappa | \Phi_i \rangle_{\boldsymbol{r}^{(b)}}$ represent the electronic dipole-matrix elements evaluated in the body frame of reference (indicated by the integration over the electronic spatial coordinates $\boldsymbol{r}^{(b)}$) as a function of internuclear distance R. Substituting the electronic target states (Equation (51)) into the electronic dipole-matrix element, we can express it as

$$\langle \Phi_f | V_\kappa | \Phi_i \rangle_{\boldsymbol{r}^{(b)}} = \sum_{l_\alpha l_\gamma} \langle X^{(f)}_{l_\alpha} Y_{l_\alpha m_\alpha} | \mathcal{P}_\kappa(\rho) Y_{1,\kappa}(\hat{\boldsymbol{\rho}}) | X^{(i)}_{l_\gamma} Y_{l_\gamma m_\gamma} \rangle_{\boldsymbol{\rho}}$$

$$= \sum_{l_\alpha l_\gamma} \int_0^\infty X^{(f)}_{l_\alpha}(\rho) J^{l_\alpha, l_\gamma}_{m_\alpha, m_\gamma}(\rho; \kappa) X^{(i)}_{l_\gamma}(\rho) d\rho, \tag{62}$$

where, for convenience, we define $J^{l_\alpha, l_\gamma}_{m_\alpha, m_\gamma}(\rho; \kappa)$ as

$$J^{l_\alpha, l_\gamma}_{m_\alpha, m_\gamma}(\rho; \kappa) = \mathcal{P}_\kappa(\rho) \langle Y_{l_\alpha m_\alpha} | Y_{1,\kappa} | Y_{l_\gamma m_\gamma} \rangle_{\hat{\boldsymbol{\rho}}}$$

$$= \mathcal{P}_\kappa(\rho) \int Y^*_{l_\alpha m_\alpha}(\hat{\boldsymbol{\rho}}) Y_{1,\kappa}(\hat{\boldsymbol{\rho}}) Y_{l_\gamma m_\gamma}(\hat{\boldsymbol{\rho}})$$

$$\times [(\rho + R/2)^2 - (R/2)^2 \eta^2] d\hat{\boldsymbol{\rho}}, \tag{63}$$

and

$$A^{l_1, l_2, l_3}_{m_1, m_2, m_3} = \sqrt{\frac{4\pi}{(2l_2 + 1)}} \langle Y_{l_1 m_1} | Y_{l_2 m_2} | Y_{l_3 m_3} \rangle_{\hat{\boldsymbol{\rho}}}$$

$$= (-1)^{l_2} C^{l_3 0}_{l_1 0, l_2 0} C^{l_1 m_1}_{l_3 m_3, l_2 m_2}, \tag{64}$$

which is derived in Zammit et al. (2017a). Hence, with Equations (62)–(64), we can express the matrix elements as

$$J^{l_\alpha, l_\gamma}_{m_\alpha, m_\gamma}(\rho; \kappa = 0) = (\rho + R/2)$$

$$\times \left[\left(\rho^2 + R\rho + \frac{R^2}{10}\right) A^{l_\alpha, 1, l_\gamma}_{m_\alpha, 0, m_\gamma} - \frac{R^2}{10} A^{l_\alpha, 3, l_\gamma}_{m_\alpha, 0, m_\gamma} \right], \tag{65}$$

$$J^{l_\alpha, l_\gamma}_{m_\alpha, m_\gamma}(\rho; \kappa = \pm 1) = \sqrt{\rho(\rho + R)}$$

$$\times \left[\left(\rho^2 + R\rho + \frac{R^2}{5}\right) A^{l_\alpha, 1, l_\gamma}_{m_\alpha, \kappa, m_\gamma} - \frac{R^2}{5\sqrt{6}} A^{l_\alpha, 3, l_\gamma}_{m_\alpha, \kappa, m_\gamma} \right]. \tag{66}$$

Then, the integration over ρ in Equation (62) is carried out numerically. The integration over the internuclear separation R in Equation (8), i.e.,

$$\mathcal{M}_{fE_{k_f}N_f, i v_i N_i} = \langle \nu_{fE_{k_f}N_f} | \{ \langle \Phi_f | V_\kappa | \Phi_i \rangle_{\boldsymbol{r}^{(b)}} \} | \nu_{i v_i N_i} \rangle_R, \tag{67}$$

is also carried out numerically.

ORCID iDs

James Colgan ⓘ https://orcid.org/0000-0003-1045-3858
David P. Kilcrease ⓘ https://orcid.org/0000-0002-2319-5934
Igor Bray ⓘ https://orcid.org/0000-0001-7554-8044
Christopher J. Fontes ⓘ https://orcid.org/0000-0003-1087-2964
Peter Hakel ⓘ https://orcid.org/0000-0002-7936-4231

References

Allard, N., Drira, I., Gerbaldi, M., Kielkopf, J., & Spielfiedel, A. 1998, A&A, 335, 1124
Allard, N. F., Kielkopf, J., Drira, I., & Schmelcher, P. 2000, EPJD, 12, 263
Allard, N. F., Noselidze, I., & Kruk, J. W. 2009, A&A, 506, 993
Argyros, J. D. 1974, JPhB, 7, 2025
Augustovičová, L., Špirko, V., Kraemer, W. P., & Soldán, P. 2013a, A&A, 553, A42
Augustovičová, L., Špirko, V., Kraemer, W. P., & Soldán, P. 2013b, MNRAS, 435, 1541
Babb, J. F. 1994, MolPh, 81, 17
Babb, J. F. 2015, ApJS, 216, 21
Babb, J. F., & Kirby, K. P. 1998, in The Molecular Astrophysics of Stars and Galaxies Vol. 4, ed. T. W. Hartquist & D. A. Williams (Oxford: Clarendon), 11
Bates, D. R. 1951a, JChPh, 19, 1122
Bates, D. R. 1951b, MNRAS, 111, 303
Bates, D. R. 1952, MNRAS, 112, 40
Bates, D. R., Darling, R. T. S., Hawe, S. C., & Stewart, A. L. 1953a, PPSL, 66, 1124
Bates, D. R., Darling, R. T. S., Hawe, S. C., & Stewart, A. L. 1954, PPSA, 67, 533
Bates, D. R., Ledsham, K., & Stewart, A. L. 1953b, RSPTA, 246, 215
Beckel, C. L., Shafi, M., & Peek, J. M. 1973, JChPh, 59, 5288
Bertoldi, F., & Draine, B. T. 1996, ApJ, 458, 222
Bishop, D., Cheung, L. M., & Buckingham, A. D. 1980, MolPh, 41, 1225
Bishop, D. M. 1990, RvMP, 62, 343
Bishop, D. M., & Cheung, L. M. 1977, PhRvA, 16, 640
Bishop, D. M., & Cheung, L. M. 1978, JPhB, 11, 3133
Bishop, D. M., & Cheung, L. M. 1979, CPL, 66, 467
Bishop, D. M., & Cheung, L. M. 1980, JChPh, 72, 5125
Brown, J. M., & Carrington, A. 2003, Rotational Spectroscopy of Diatomic Molecules (Cambridge: Cambridge Univ. Press)
Carrington, A., McNab, I. R., & Montgomerie, C. A. 1989, CPL, 160, 237
Coppola, C. M., Longo, S., Capitelli, M., Palla, F., & Galli, D. 2011, ApJS, 193, 7
Coppola, C. M., Mizzi, G., Bruno, D., et al. 2016, MNRAS, 457, 3732
Critchley, A. D. J., Hughes, A. N., & McNab, I. R. 2001, PhRvL, 86, 1725
Dalgarno, A., & Lewis, J. T. 1957, RSPSA, 240, 284
Dance, D. F., Harrison, M. F. A., Rundel, R. D., & Smith, A. C. H. 1967, PPS, 92, 577
Draine, B. T., & Bertoldi, F. 1996, ApJ, 468, 269
Dunn, G. H. 1968, PhRv, 172, 1
Dunn, G. H., & Van Zyl, B. 1967, PhRv, 154, 40
Fabian, A. C., Johnstone, R. M., Sanders, J. S., et al. 2008, Natur, 454, 968
Ferland, G. J., Porter, R. L., van Hoof, P. A. M., et al. 2013, RMxAA, 49, 137
Galli, D., & Palla, F. 1998, A&A, 335, 403
Ghazaly, M. O. A. E., Jureta, J., Urbain, X., & Defrance, P. 2004, JPhB, 37, 2467
Gianturco, F. A., & Giorgi, P. G. 1997, ApJ, 479, 560
Glover, S. C. O., Chluba, J., Furlanetto, S. R., Pritchard, J. R., & Savin, D. W. 2014, AAMOP, 63, 135
Haiman, Z., Rees, M. J., & Loeb, A. 1996, ApJ, 467, 522
Hansson, A., & Watson, J. K. 2005, JMoSp, 233, 169
Haxton, D. J. 2013, PhRvA, 88, 013415

Herzberg, G. 1950, Molecular Spectra and Molecular Structure I. Spectra of Diatomic Molecules (2nd ed.; Princeton, NJ: D. Van Norstrand Company Inc)
Hester, J. J. 2008, ARA&A, 46, 127
Hirata, C. M., & Padmanabhan, N. 2006, MNRAS, 372, 1175
Hunter, G., Yau, A. W., & Pritchard, H. O. 1974, ADNDT, 14, 11
Igarashi, A. 2014, EPJD, 68, 266
Janev, R., Reiter, D., & Samm, U. 2003, Collision Processes in Low-Temperature Hydrogen Plasmas (Jülich: EIRENE), http://www.eirene.de/report_4105.pdf
Kang, H., & Shapiro, P. R. 1992, ApJ, 386, 432
Kitayama, T., Susa, H., Umemura, M., & Ikeuchi, S. 2001, MNRAS, 326, 1353
Koyama, H., & Inutsuka, S.-I. 2000, ApJ, 532, 980
Latter, W. B., & Black, J. H. 1991, ApJ, 372, 161
Lebedev, V. S., & Presnyakov, L. P. 2002, JPhB, 35, 4347
Lebedev, V. S., Presnyakov, L. P., & Sobel'man, I. I. 2003, PhyU, 46, A02
Lepp, S., Stancil, P. C., & Dalgarno, A. 2002, JPhB, 35, R57
Light, J. C., Ross, K. P., & Shuler, K. E. 1969, in Kinetic Processes in Gases and Plasmas, ed. A. R. Hochstim (New York: Academic), 281
Loh, E. D., Baldwin, J. A., Curtis, Z. K., et al. 2011, ApJS, 194, 30
Loh, E. D., Baldwin, J. A., & Ferland, G. J. 2010, ApJL, 716, L9
Longo, S., Coppola, C. M., Galli, D., Palla, F., & Capitelli, M. 2011, Rend. Fis. Acc. Lincei, 22, 119
Lykins, M. L., Ferland, G. J., Kisielius, R., et al. 2015, ApJ, 807, 118
Mac Low, M.-M., & Shull, J. M. 1986, ApJ, 302, 585
Madsen, M. M., & Peek, J. M. 1971, ADNDT, 2, 171
Mayer, M., & Duschl, W. J. 2005, MNRAS, 358, 614
Mihajlov, A. A., Ignjatović, L. M., Sakan, N. M., & Dimitrijević, M. S. 2007, A&A, 469, 749
Mitroy, J., Safronova, M. S., & Clark, C. W. 2010, JPhB, 43, 202001
Morrison, M. A., & Sun, W. 1995, in Computational Methods for Electron-molecule Collisions, ed. W. M. Huo & F. A. Gianturco (New York: Plenum), 131
O'Shea, B. W., & Norman, M. L. 2008, ApJ, 673, 14
Omukai, K. 2001, ApJ, 546, 635
Peek, J. M. 1974, PhRvA, 10, 539
Pelisoli, I., Santos, M. G., & Kepler, S. O. 2015, MNRAS, 448, 2332
Pitchford, L. C., Alves, L. L., Bartschat, K., et al. 2016, Plasma Process. Polym., 14, 1600098

Ramaker, D. E., & Peek, J. M. 1973, ADNDT, 5, 167
Ramaker, D. E., & Peek, J. M. 1976, PhRvA, 13, 58
Richardson, C. T., Baldwin, J. A., Ferland, G. J., et al. 2013, MNRAS, 430, 1257
Saha, S., Datta, K. K., Basu, D., & Barua, A. K. 1980, JPhB, 13, 3755
Santos, M. G., & Kepler, S. O. 2012, MNRAS, 423, 68
Shapiro, P. R., & Kang, H. 1987, ApJ, 318, 32
Sobel'man, I. I. 1972, Introduction to the Theory of Atomic Spectra (New York: Pergamon)
Sonnleitner, S. A., Beckel, C. L., & Peek, J. M. 1996, JChPh, 104, 2801
Stancil, P. 1994a, JQSRT, 51, 655
Stancil, P. C. 1994b, ApJ, 430, 360
Stancil, P. C., Babb, J. F., & Dalgarno, A. 1993, ApJ, 414, 672
Stancil, P. C., Lepp, S., & Dalgarno, A. 1998, ApJ, 509, 1
Sugimura, K., Coppola, C. M., Omukai, K., Galli, D., & Palla, F. 2016, MNRAS, 456, 270
Susa, H., & Kitayama, T. 2000, MNRAS, 317, 175
Susa, H., & Umemura, M. 2006, ApJL, 645, L93
Tsogbayar, T., & Banzragch, T. 2010, arXiv:1007.4354
van Dishoeck, E. F. 1987, JChPh, 86, 196
van Dishoeck, E. F., & Dalgarno, A. 1983, JChPh, 79, 873
Varshalovich, D. A., Moskalev, A. N., & Khersonskii, V. K. 1988, Quantum Theory of Angular Momentum (1st ed.; Philadelphia, PA: World Scientific)
Victor, G. A., & Dalgarno, A. 1969, JChPh, 50, 2535
von Busch, F., & Dunn, G. H. 1972, PhRvA, 5, 1726
Vujčić, V., Jevremović, D., Mihajlov, A. A., et al. 2015, JApA, 36, 693
Watson, J. K. 2008, JMoSp, 252, 5
Whiting, E. E., & Nicholls, R. W. 1974, ApJS, 27, 1
Yoshida, N., Abel, T., Hernquist, L., & Sugiyama, N. 2003, ApJ, 592, 645
Yoshida, N., Oh, S. P., Kitayama, T., & Hernquist, L. 2007, ApJ, 663, 687
Zámečníková, M., Kraemer, W. P., & Soldán, P. 2017, JQSRT, 191, 88
Zammit, M. C., Fursa, D. V., & Bray, I. 2013, PhRvA, 88, 062709
Zammit, M. C., Fursa, D. V., & Bray, I. 2014, PhRvA, 90, 022711
Zammit, M. C., Fursa, D. V., Savage, J. S., & Bray, I. 2017a, JPhB, 50, 123001
Zammit, M. C., Savage, J. S., Fursa, D. V., & Bray, I. 2016, PhRvL, 116, 233201
Zammit, M. C., Savage, J. S., Fursa, D. V., & Bray, I. 2017b, PhRvA, 95, 022708